

1 **Reconstructing seasonality through stable isotope and trace element analysis of the Proserpine**
2 **stalagmite, Han-sur-Lesse Cave, Belgium: indications for climate-driven changes during the last 400**
3 **years**

4 Stef Vansteenberge^{1*}, Niels J. de Winter¹, Matthias Sinnesael¹, Sophie Verheyden^{2,1}, Steven Goderis¹,
5 Stijn J. M. Van Malderen³, Frank Vanhaecke³ and Philippe Claeys¹.

6 ¹Department of Analytical, Environmental and Geochemistry, Vrije Universiteit Brussel, Pleinlaan 2, B-
7 1050 Brussels, Belgium.

8 ²Royal Belgian Institute of Natural Sciences, Jennerstraat 13, B- 1000 Brussels, Belgium

9 ³Department of Analytical Chemistry, Ghent University, Campus Sterre, Krijgslaan 281 S12, B-9000
10 Ghent, Belgium

11 ***Corresponding author: Niels.de.winter@vub.be**

12

13 **Abstract**

14 Fast growing speleothems allow the reconstruction of palaeoclimate down to a seasonal scale.
15 Additionally, annual lamination in some of these speleothems yields highly accurate age models for
16 these palaeoclimate records, making these speleothems valuable archives for terrestrial climate. In
17 this study, an annually laminated stalagmite from the Han-sur-Lesse Cave (Belgium) is used to study
18 the expression of the seasonal cycle in northwestern Europe during the Little Ice Age. More specifically,
19 two historical 12-year-long growth periods (ca. 1593-1605 CE and 1635-1646 CE) and one modern
20 growth period (1960-2010 CE) are analyzed on a sub-annual scale for their stable isotope ratios ($\delta^{13}\text{C}$
21 and $\delta^{18}\text{O}$) and trace element (Mg, Sr, Ba, Zn, Y, Pb, U) content. Seasonal variability in these proxies is
22 confirmed with frequency analysis. Zn, Y and Pb show distinct annual peaks in all three investigated
23 periods related to annual flushing of the soil during winter. A strong seasonal in phase relationship
24 between Mg, Sr and Ba in the modern growth period reflects a substantial influence of enhanced prior
25 calcite precipitation (PCP). In particular, PCP occurs during summers when recharge of the epikarst is
26 low. This is also evidenced by earlier observations of increased $\delta^{13}\text{C}$ values during summer. In the 17th
27 century intervals, there is a distinct antiphase relationship between Mg, Sr and Ba, suggesting that
28 processes other than PCP, i.e. varying degrees of incongruent dissolution of dolomite, eventually
29 related to changes in soil activity and/or land use change are more dominant. The processes controlling
30 seasonal variations in Mg, Sr and Ba in the speleothem appear to change between the 17th century and
31 1960-2010 CE. The Zn, Y, Pb and U concentration profiles, stable isotope ratios and morphology of the

32 speleothem laminae all point towards increased seasonal amplitude in cave hydrology. Higher seasonal
33 peaks in soil-derived elements (e.g. Zn and Y) and lower concentrations of host-rock derived elements
34 (e.g. Mg, Sr, Ba) point towards lower residence times in the epikarst and higher flushing rates during
35 the 17th century. These observations reflect an increase in water excess above the cave and recharge
36 of the epikarst, due to a combination of lower summer temperatures and increased winter
37 precipitation during the 17th century. This study indicates that the transfer function controlling Mg, Sr
38 and Ba seasonal variability varies over time. Which process is dominant, either PCP. Soil activity or
39 dolomite dissolution, is clearly climate-driven and can itself be used as a paleoenvironment proxy.

40 **Keywords:** Speleothem, seasonality, Little Ice Age, trace element concentrations, stable isotope ratios,
41 proxy transfer functions

42 **1. Introduction**

43 Speleothems have been successfully used to reconstruct paleoclimate on various time scales (Fairchild
44 and Baker, 2012), from tropical latitudes (e.g. Wang et al., 2001) to temperate areas (e.g. Genty et al.,
45 2003). Fast growing speleothems enable paleoclimate reconstructions to reach seasonal resolution, or
46 even higher (Van Rangelbergh et al., 2014). Some speleothems are characterized by distinct physical
47 and/or geochemical layering, which improves chronologies and lends more confidence to the
48 interpretation of proxy records at these high temporal resolutions (e.g. Matthey et al., 2008; Boch &
49 Spötl, 2008). The occurrence of visible annual laminae in speleothems has been reported from sites all
50 over the world (Baker et al., 2008). A common expression of this visible layering is an alternation of
51 dark compact laminae (DCL) and white porous laminae (WPL), as defined by Genty and Quinif (1996).
52 According to Dreybrodt (1999) and Baker et al. (2008), the origin of visible seasonal layering is related
53 to seasonal variations in drip rate and in drip water supersaturation. Additionally, seasonal changes in
54 cave ventilation can influence the intensity of the degassing process of the dripwater and influence the
55 pH of the fluid from which the speleothem precipitates, producing seasonal variations in crystal fabric
56 (e.g. Frisia et al., 2003). These two processes can work in conjunction, with drip rate influencing annual
57 laminae thickness while degassing influences the speleothem fabric (Boch et al., 2010). Such changes
58 in drip rate often coincide with the presence of a varying degree of prior calcite precipitation (PCP).
59 PCP is the process of calcite precipitation upstream of the site of speleothem deposition (Fairchild et
60 al., 2000). An increase in PCP occurs when the ability of infiltration waters to degas increases.
61 Therefore, a higher degree of PCP is attributed to drier periods (Fairchild et al., 2000; Fairchild and
62 Treble, 2009). Variations in the amount of PCP have been observed on a seasonal scale (e.g. Johnson
63 et al., 2006).

64 The presence of seasonally laminated speleothems in Belgian cave systems has been known for several
65 decades (e.g. Genty and Quinif, 1996). The best known example is the Proserpine stalagmite, which
66 was cored in the cave of Han-sur-Lesse and first studied by Verheyden et al. (2006). The speleothem
67 has a well-expressed visual and geochemical seasonal layering over the last 500 years as inferred from
68 and U/Th dating and lamina counting between the radiometric ages (Van Rampelbergh et al., 2015).
69 This geochemical layering is reflected by sub-annual variations of stable isotope ratios ($\delta^{13}\text{C}$ and $\delta^{18}\text{O}$).
70 A thorough understanding of modern seasonal control on variations in $\delta^{13}\text{C}$ and $\delta^{18}\text{O}$ in speleothem
71 calcium carbonate results from rigorous monitoring of the conditions at the sample site in Han-sur-
72 Lesse cave as carried out by Van Rampelbergh et al. (2014) for the period 2012-2014.

73 In addition to the commonly used speleothem $\delta^{18}\text{O}$ and $\delta^{13}\text{C}$ proxies, the use of trace elemental
74 concentrations (e.g. Mg, Sr, Ba, Zn and U) as palaeoclimate and palaeoenvironmental proxies is
75 becoming standard practice in speleothem reconstructions (Fairchild et al., 2000; Treble et al., 2003;
76 Fairchild and Treble, 2009; Griffiths et al., 2010; Regattieri et al., 2016). The use of trace elements
77 brings additional information that can be used to unravel seasonal variability in speleothem chemistry.
78 Examples of this include the use of trace element concentrations as proxies for precipitation (Baldini
79 et al., 2002; Warken et al., 2018), soil processes (Regattieri et al., 2016) or changes in sediment supply
80 (Regattieri et al., 2016). They have also been linked to changes in the atmospheric load of
81 anthropogenic and volcanic derived aerosols, as well as volcanic ash fall events from speleothem
82 records (Frisia et al., 2005; Jamieson et al., 2015).

83 The first objective of this study is to better characterize the geochemical layering of the Proserpine
84 speleothem by adding trace element proxies to improve the understanding of processes driving the
85 geochemical layering and to further resolve its relation with seasonal climatic variability. In addition,
86 the present study compares the seasonal cycle within earlier identified cold periods (Verheyden et al.,
87 2006; Van Rampelbergh et al., 2015; Supp. Mat. **Fig. 1**) to present-day seasonal signals. To achieve this,
88 two 12-year long stalagmite growth periods (1593-1605 CE \pm 30, hereafter P16 and 1635-1646 CE \pm 30,
89 hereafter P17) and a more recent growth period deposited between 1960-2010 CE (hereafter referred
90 to as P20) were analysed at a sub-annual scale for their stable isotopic ($\delta^{13}\text{C}$ and $\delta^{18}\text{O}$) and trace
91 element variations. The names of these growth periods (roughly) refer to the century in which they
92 were deposited (16th, 17th and 20th century respectively). Chemical changes in these three intervals will
93 be interpreted in the context of the longer stable isotope record that is available from Van
94 Rampelbergh et al. (2015) to discuss changes in hydroclimate and seasonality over the past 500 years
95 as recorded in the Proserpine speleothem.

96 **2. Geological setting**

97 **2.1 Han-sur-Lesse Cave**

98 With a total length of approximately 10 km, the Han-sur-Lesse Cave system, located within a limestone
99 belt of Middle Devonian age, is the largest known subterranean karst network in Belgium (**Fig. 1A**). The
100 cave system was formed by a meander cut-off of the Lesse River within the Massif de Boine, which is
101 part of an anticline structure consisting of Middle to Late Givetian reefal limestones (i.e. the Mont-
102 d'Hours and Fromelennes Formations (Fm); Delvaux de Fenffe, 1985; **Fig. 1C**). The limestone epikarst
103 reaches a thickness of 20-50 m above the cave, as estimated by the map of the cave and the surface.
104 (Quinif, 1988). Studies have shown the presence of dolomite in these Givetian limestones which are
105 directly overlying the Han-sur-Lesse cave (**Fig. 1**). Within the Mont-d'Hours Fm., the biostromal
106 limestones are alternated with fine-grained micritic limestones and dolomitic shales (Preat et al.,
107 2006). Additionally, studies by Verheyden et al. (2000) and Pas et al. (2016) on the Middle Devonian
108 strata in which the Han-sur-Lesse cave is situated have shown that dolomitized beds also occur within
109 the limestones of the Fromelennes Fm. Specifically, the Salle du Dôme, in which the Proserpine is
110 located, opens in the Devonian Givetian limestone beds forming an anticline structure, which explains
111 the surface geomorphology of the hill in which the cave is located (Delvaux de Fenffe, 1985; **Fig. 1**).
112 Since no impermeable formations are present above the cave, precipitation directly seeps through the
113 thin (~25 cm) soil and enters the epikarst.

114 The Han-sur-Lesse Cave is located ~200 km inland at an elevation of 200 m above sea level. The region
115 is marked by a warm temperate, fully humid climate with cool summers, following the Köppen-Geiger
116 classification (Kottek et al., 2006). In the period 1999-2012, the region experienced a seasonality in
117 monthly temperatures between 2.5°C (January) and 18°C (July), with a mean annual temperature of
118 10.2 °C (**Fig. 2**). Precipitation is fairly constant year round around 40-50 mm month⁻¹, with two months
119 (July and August) experiencing increased precipitation of 90-95 mm month⁻¹. Mean annual
120 precipitation was 820 mm yr⁻¹ in Rochefort, 10 km from Han-sur-Lesse (Royal Belgian Meteorological
121 Institute, Brussels, Belgium). The study site is affected by a North Atlantic moisture source all year
122 round (Gimeno et al., 2010) and the amount of precipitation does not follow a seasonal distribution.
123 Calculations applying the Thornthwaite formula (Thornthwaite and Mater, 1957) show that there is a
124 strong seasonal trend in the water excess, i.e. the amount of rainfall minus the amount lost by
125 evapotranspiration, with water excess only occurring from October to April (Genty and Deflandre,
126 1998; Genty and Quinif, 1996).

127 The studied speleothem was retrieved from the Salle-du-Dôme in 2001, a 150 m wide and 60 m high
128 chamber that formed by roof-collapse of the limestone (**Fig 1B**). The Salle-du-Dôme is well ventilated,
129 as it is located close to the cave exit and connected through two passages to nearby chambers.

130 Monitoring of cave atmosphere within the Salle-du-Dôme for the period 2012-2014 showed that in
131 2013 the temperature inside the chamber varied seasonally between 10.5 and 14.5 °C (Van
132 Rampelbergh et al., 2014). Similar seasonal trends in temperature are observed for drip water sampled
133 at the site of the Proserpine speleothem, but the mean is 0.5 °C colder than the outside air
134 temperature. The pCO₂ of the cave air fluctuates between 400 ppmv and 1000 ppmv (in July and
135 August), and averages 500 ppmV during the year. In summer (July-August), a rapid and temporary (2
136 month) increase to 1000 ppmV is observed. Also during summer, rainwater δ¹⁸O and δD above the
137 cave increase by 3 ‰ and 30 ‰ (VSMOW, Vienna Standard Mean Ocean Water) respectively, likely
138 due to the atmospheric temperature effect as described by Rozanski et al. (1992). In contrast, drip
139 water δ¹⁸O and δD remain fairly stable throughout the year, with means of -7.65 ‰ and -50.1 ‰
140 VSMOW and standard deviations of 0.07 ‰ and 0.6 ‰ VSMOW, respectively. During late summer
141 (September), an increase of 1.5 ‰ is observed in the δ¹³C values of dissolved inorganic carbon (DIC)
142 within the drip water

143 **2.2 Proserpine speleothem**

144 The Proserpine speleothem is a 2 m high, stalagmitic flowstone with a flat top. The speleothem has a
145 surface area of 1.77 m² and is fed by a drip flow with drip rates ranging between 100 and 300 mL min⁻¹.
146 The type of speleothem is described in the literature as a “tam-tam speleothem” and is characterized
147 by the occurrence of millimetre to centimetre scale rimmed pools, which causes chaotic “pool-like”
148 deposits to occur in parts of the speleothem (Verheyden et al., 2006). The speleothem grew over a
149 period of approximately 2 kyr and thus has an exceptionally high mean growth rate of 1 mm yr⁻¹. This
150 large speleothem was drilled and a 2 m long core was retrieved. The upper 50 cm of this core, dating
151 back to approximately 1500 CE (Supp. Mat. Fig. 2), shows a well-expressed layering of alternating Dark
152 Compact Layers (DCL) and White Porous Layers (WPL; Verheyden et al., 2006). Previous studies
153 concluded that simultaneous multi-decadal changes in different proxies (such as crystal fabric, growth
154 rate, layer thickness, and oxygen and carbon stable isotope ratios) indicate that these are controlled
155 by climatic, environmental or anthropogenic factors, and that some parts of the Proserpine
156 speleothem have been deposited out of isotopic equilibrium with the drip water (Verheyden et al.,
157 2006; Van Rampelbergh et al., 2015).

158 Based on a detailed cave monitoring study at the Proserpine site in the years 2012 to 2014, Van
159 Rampelbergh et al. (2014) showed that δ¹⁸O and δ¹³C of seasonally deposited calcite reflect isotopic
160 equilibrium conditions and that variations of stable isotope ratios are induced by seasonal changes.
161 These seasonal changes in stable isotope ratios correspond with the observed visible layering. The
162 speleothem δ¹⁸O value is believed to reflect changes in seasonal cave climatology. While drip water

163 $\delta^{18}\text{O}$ remains constant, calcite $\delta^{18}\text{O}$ decreases by $\sim 0.6\text{‰}$ in summer months, caused by temperature-
164 dependent fractionation during calcite precipitation. This fractionation was calculated to be $-0.2\text{‰}\text{ }^{\circ}\text{C}^{-1}$
165 ¹ (Van Rampelbergh et al., 2014). In contrast, $\delta^{13}\text{C}$ reflects seasonal changes occurring at the epikarst
166 level. A $\sim 1.5\text{‰}$ increase of $\delta^{13}\text{C}$ in drip water DIC during late summer is directly reflected in the freshly
167 deposited speleothem calcite. The enrichment in drip water $\delta^{13}\text{C}$ values occurs shortly after the
168 observed decrease in drip water discharge, and therefore seasonal variations in the degree of prior
169 calcite precipitation in the epikarst has been hypothesized to be the main driver of seasonal $\delta^{13}\text{C}$
170 changes in the drip water (Van Rampelbergh et al., 2014).

171 **2.3 Dating**

172 The age-depth model of the Proserpine speleothem core has been established and discussed by Van
173 Rampelbergh et al. (2015) and is provided in the supplementary material (Supp. Mat. Fig. 2). This age-
174 depth model was constructed by using a combined approach of U-Th radiometric dating, based on 20
175 U-Th ages, and layer counting. It was shown that the number of counted layers is in good agreement
176 with the U-Th ages (see **Table 1** in Van Rampelbergh et al., 2015). However, 9 to 10 cm from the top
177 of the core, a perturbation with heavily disturbed calcite occurs, making it impossible to construct a
178 continuous layer counting chronology. Remains of straw and soot were found within this perturbation,
179 suggesting that at that time, fires were lit on the speleothem's palaeosurface (Verheyden et al., 2006).
180 Layer counting gave an age of 1857 ± 6 CE for the reestablishment of calcite deposition after the
181 perturbation and U-Th age-depth modeling showed that the start of the perturbation occurred at 1810
182 ± 45 CE (Van Rampelbergh et al., 2015). Radiocarbon dating of the straw fragments embedded in the
183 calcite gave an age between 1760 and 1810 CE, with 95.4 % probability. The age of 1810 ± 45 CE is
184 used to restart the layer counting after the perturbation towards the bottom of the core. This gave an
185 age of 1593 to 1605 ± 30 CE for the P16 and 1635 to 1646 ± 30 CE for the P17 section. The more recent
186 section P20 studied here is situated above the perturbation and its age could be confidently
187 established through annual layer counting between 1960 and 2001 CE. The same chronology for the
188 Proserpine speleothem was previously used in conjunction with petrographic evidence to show that
189 decreases in cave visitation coincided with the two World Wars, highlighting the accuracy of the age
190 model (Verheyden et al., 2006).

191

192 **3. Methods**

193 **3.1 Analytical procedures**

194 The three growth periods studied are shown in **Fig. 3** and their age is derived from an age-depth model
195 based on U-Th-dating and layer counting (Verheyden et al., 2006; Van Rampelbergh et al., 2015; Fig.
196 S5; see **2.3**). The number of counted layer couplets over the annually layered 500-years determined
197 the seasonal character of the layers and demonstrated that two layers (one DCL and a WPL) were
198 deposited per year. The number of years obtained by layer counting between two U-Th datings was
199 compared with the number of years suggested by the U-Th ages. We combine results of both
200 independent dating methods to produce the final age model. All growth transects are sampled parallel
201 to the local direction of growth of the Proserpine speleothem and perpendicular to the growth laminae
202 (see **Fig. 2**).

203 For $\delta^{13}\text{C}$ and $\delta^{18}\text{O}$ analysis, powder samples were acquired with a Merchantek Micromill
204 (Merchantek/Electro Scientific Industries Inc. (ESI), Portland (OR), USA, coupled to a Leica GZ6, Leica
205 Microsystems GmbH, Wetzlar, Germany) equipped with tungsten carbide dental drills with a drill bit
206 diameter of 300 μm . The powders are stored in a 50 °C oven prior the analysis to avoid $\delta^{13}\text{C}$ and $\delta^{18}\text{O}$
207 isotopic contamination. Measurements for P16 and P17 are carried out on a Nu Perspective isotope
208 ratio mass spectrometer (IRMS) coupled to a Nucarb automated carbonate preparation device (Nu
209 Instruments, UK) at the Vrije Universiteit Brussel (Belgium). The $\delta^{13}\text{C}$ and $\delta^{18}\text{O}$ records of P16 and P17
210 consist of 201 and 116 data points, respectively, resulting in temporal resolutions of ~ 20 and ~ 10 data
211 points per year, respectively. The analysis of the P20 interval is an extension of the previously published
212 seasonally resolved 1976-1985 transect (Van Rampelbergh et al., 2014) and was carried out on a Delta
213 plus XL IRMS coupled to a Kiel III carbonate preparation unit (Thermo Fisher Scientific, Germany) also
214 at the Vrije Universiteit Brussel. For P20, a total of 350 samples were analysed, providing a temporal
215 resolution of ~ 7 data points per year. All results are displayed as ‰VPDB (Vienna Pee Dee Belemnite)
216 with the individual reproducibility reported as 2 standard deviation (SD) uncertainties. Within each
217 batch of ten samples, the in-house reference material MAR2-2, prepared from Marbella limestone and
218 calibrated against NBS-19 (Friedman et al., 1982) is measured together with the samples to correct for
219 instrumental drift ($\delta^{13}\text{C}$: 3.41 ± 0.10 ‰ (2 SD) VPDB; $\delta^{18}\text{O}$: 0.13 ± 0.20 ‰ (2 SD) VPDB). Total
220 uncertainties for $\delta^{13}\text{C}$ and $\delta^{18}\text{O}$ are 0.03 ‰ and 0.09 ‰ (1 SD) for the Nu Perspective setup. With the
221 Delta plus XL setup these are slightly higher, being 0.04 ‰ and 0.10 ‰ for $\delta^{13}\text{C}$ and $\delta^{18}\text{O}$, respectively
222 (Van Rampelbergh et al., 2014).

223 Trace element variations are determined using inductively coupled plasma-mass spectrometry
224 complemented by a laser ablation sample introduction system (LA-ICP-MS) at Ghent University
225 (Belgium). The LA-ICP-MS setup consists of a 193 nm ArF*excimer Analyte G2 laser ablation system
226 (Teledyne Photon Machines, Bozeman, MT, USA) coupled to a single-collector sector field 'Element XR'
227 ICP-MS unit (Thermo Fisher Scientific, Bremen, Germany). The laser was used to sample adjacent

228 positions along a line segment parallel to the growth axis. The positions were ablated one-by-one for
229 15 s with a laser spot size of 50 μm in diameter, a repetition rate of 30 Hz and a beam energy density
230 of 3.51 J cm^{-2} . The line segments for P16, P17 and P20 are drilled at 287, 249 and 445 individual
231 positions, respectively. Sampling via individual laser spots was preferred over the conventional
232 approach of continuous line scanning because the single positions can be sampled longer, resulting in
233 an improved limit of detection. To carry out the analyses, the speleothem sections and reference
234 materials were mounted in a HELEX 2 double-volume ablation cell. The Helium carrier gas (0.5 L min^{-1})
235 is mixed with Argon make-up gas (0.9 L min^{-1}) downstream of the ablation cell, and introduced into the
236 ICP-MS unit, operated in low mass-resolution mode. Transient signals for magnesium (Mg), aluminium
237 (Al), silicon (Si), phosphorus (P), sulphur (S), potassium (K), iron (Fe), manganese (Mn), zinc (Zn),
238 rubidium (Rb), strontium (Sr), yttrium (Y), barium (Ba), lead (Pb), thorium (Th), and uranium (U) were
239 monitored during analysis of the laser-induced aerosol. Cool plasma conditions (800 W RF power) are
240 used to reduce Argon-based interferences and to increase the sensitivity of the analysis. A gas blank
241 subtraction is performed on the data acquired at each position, based on the signal acquired 10 s prior
242 to the ablation. Precise and accurate trace element concentration data were obtained from offline
243 calibration, using seven international natural and synthetic glass and carbonate reference materials:
244 BHVO-2G, BIR-1G, GSD-1G, GSE-1G, and MACS-3 (United States Geological Survey) as well as SRM 610
245 and 612 (National Institute of Standards and Technology). Ca is used as an internal standard for
246 calibration of the speleothem measurements, following the assumption that the calcium carbonate in
247 the speleothem contains 38 wt. % Ca. Based on the reference materials and settings described, the
248 reproducibility of the produced elemental concentration data was typically on the order of 5% relative
249 standard deviation (RSD). Limits of detection (LODs) are given in **Table 2**.

250 **3.2 Data Processing**

251 Frequency analysis is applied to study the variations in the different proxy signals, and allows
252 evaluating which of these proxies fluctuate seasonally. The benefit of frequency analysis for assessing
253 seasonal cyclicity in a proxy in speleothems and other incremental climate archives was already
254 recognized by Smith et al. (2009) and de Winter et al. (2017). Furthermore, the method can identify
255 multi-annual trends or variability at the sub-seasonal level. Frequency analysis is performed using Fast
256 Fourier Transformations (FFT) of the isotopic and trace element data in the distance domain. The data
257 were detrended and padded with zeros. The power spectra were plotted as simple periodograms with
258 frequencies in the distance domain (mm^{-1}) to allow interpretation of seasonality in the data. The
259 significance level (95%) was evaluated using Monte Carlo noise simulations. The routine used operates
260 in MATLAB® and was based on the scripts provided in Muller and MacDonald (2000; see Bice et al.
261 2012 for more detail).

262

263 An effective method to compare sub-annual variations of different proxies with each other is by
264 resampling multiple annual cycles at a regular interval and stacking the individual cycles (Treble et al.,
265 2003; Johnson et al., 2006; Borsato et al., 2007; de Winter et al. 2018). The advantage of this method
266 is that the phase-relations of the different proxies are preserved (Treble et al., 2003). Annual stacks
267 are created based on moving averages to diminish the influence of low-frequency noise on the annual
268 stacks. The number of points used for moving averages is determined as a function of the sampling
269 resolution (i.e., 3-point moving average for stable isotope records and 5-point moving average for trace
270 element records, see **Fig. 4**). Proxy records with well-constrained seasonal variation are used to define
271 seasonal cycles. In this study, individual years were selected based on $\delta^{13}\text{C}$ (minima) for stable isotope
272 records and Zn (maxima) for the trace element records. Stable isotope ratios and trace element stacks
273 were created separately (**Fig. 3**). For P16 and P17, all annual cycles were included in the stack, except
274 for the first and the last one, since there was no guarantee that these are entirely represented in the
275 record. For P20, only ten years were selected from the full record to avoid the effect of multi-decadal
276 variability (see **Fig. 2**) and to maintain an approach similar to that of P16 and P17. The years are
277 indicated by the red line in **Fig. 4**.

278 **4. Results**

279 The concentration range of each proxy measured in the three different intervals is shown in **Fig. 5**. For
280 $\delta^{13}\text{C}$ and $\delta^{18}\text{O}$, the mean values and ranges (minima to maxima) in P20 are significantly higher than
281 those in P17 and P16. To illustrate the spread in the trace element records, the median was used
282 instead of the mean as the median is less sensitive to large concentration ranges and outliers. Al, Si, K,
283 Mn, Rb and Th are not included in this study since > 25% of the data falls below the LOD. An exception
284 was made in the case of Y of which only few data points are retained for P17 (81% of the data is < LOD)
285 and 18% and 36% of the data is < LOD in P20 and P16 respectively. However, Y data are discussed
286 because of the clear seasonal signal shown in P20 and P16 (Supp. Mat. Fig. 3 and 5).

287 Records of stable isotope ratios ($\delta^{13}\text{C}$ and $\delta^{18}\text{O}$) and trace element (Mg, P, Zn, Sr, Y, Ba, Pb and U)
288 concentrations are plotted against distance in **Fig. 4**. The occurrence of darker laminae (DCL) in the
289 samples is indicated by blue bands, clearly showing that these annual laminae are thicker in P16 and
290 P17 (mean 1.135 mm and 1.096 mm, respectively) compared to P20 (mean 0.382 mm). For all intervals,
291 the seasonal cycles are well constrained by $\delta^{13}\text{C}$, with lower $\delta^{13}\text{C}$ values occurring in DCL. Van
292 Rampelbergh et al. (2014) present in their figure 4, the correspondence between stable isotopic
293 compositions of the calcite samples taken by a micromill on a regular spatial sampling interval and a
294 scan of the stalagmite. This correspondence is based on the information available in 2014 and 2015.

295 However, more recent tools combined with the study of a larger portion of the stalagmite
296 demonstrates that contrary to the affirmation of Van Rampelbergh et al, (2014; 2015), lower values in
297 $\delta^{13}\text{C}$ are found in the DCL. The mean $\delta^{13}\text{C}$ is higher for P20 (-8.36 ‰) compared to P17 and P16 (-9.82
298 ‰ and -10.04 ‰, respectively). In addition, the amplitude of the individual cycles is larger in P20.
299 Seasonal cycles in $\delta^{18}\text{O}$ are much less pronounced. The most distinctive cycles are observed in P20 and
300 some can be identified in parts of P17 and P16 (e.g. between 4 and 7 mm in P16 or between 3 and 7
301 mm in P17), while for other parts (e.g. between 7 and 11 mm in P16) they appear to be absent.

302 Seasonal variations are observed for Mg, Sr and Ba in all three intervals investigated (**Fig. 4**). In P17
303 and P16, the median concentrations of these elements are similar; 447 and 444 $\mu\text{g g}^{-1}$ for Mg, 51 and
304 45 $\mu\text{g g}^{-1}$ for Sr and 36 and 33 $\mu\text{g g}^{-1}$ for Ba (**Fig. 5**). However, in P20 concentrations of Mg and Ba are
305 slightly higher compared to the older intervals, i.e. 706 $\mu\text{g g}^{-1}$ for Mg and 46 $\mu\text{g g}^{-1}$ for Ba. This is also
306 the case for Pb and U with concentrations significantly lower in P17 (0.14 and 0.05 $\mu\text{g g}^{-1}$, respectively)
307 and P16 (0.14 and 0.07 $\mu\text{g g}^{-1}$, respectively) and a seasonal cycle that is less pronounced than in P20
308 (0.37 and 0.18 $\mu\text{g g}^{-1}$). In contrast, P16 has the highest median concentrations of Zn (54 $\mu\text{g g}^{-1}$) and Y
309 (0.04 $\mu\text{g g}^{-1}$) and both elements display a well-defined seasonal covariation. Note that seasonal
310 variability in trace elements in P16 is most pronounced in the first 9 mm, after which the amplitude of
311 variability decreases. The same is not observed in the stable isotope records. Although the
312 concentration of Zn is lower in P20 and P17 (14 and 25 $\mu\text{g g}^{-1}$, respectively), the seasonal cycle is still
313 present. Similar observations can be made for Y in P20 (0.02 $\mu\text{g g}^{-1}$). Within P16 and P17, maxima of
314 Zn, Y, Sr and Ba mostly occur within the DCL.

315 **Figure 6** shows an example of the FFT periodograms of $\delta^{13}\text{C}$, Mg, Zn and P in P16. Additional
316 periodograms for the other elements in P16, P17 and P20 are included as supplementary data (Supp.
317 Mat. Fig. 3-5). The frequency analysis confirms the clear seasonal cyclicity of $\delta^{13}\text{C}$ previously observed
318 by Van Rampelbergh et al. (2014; **Fig. 6**). The dominant frequency of $\delta^{13}\text{C}$ in P16 is 0.8 mm^{-1} (**Fig. 6**).
319 This corresponds to a period of 1.25 mm, which is in good agreement with an observed mean layer
320 thickness of 1.13 mm (Supp. Mat. Fig. 6). Growth rates based on neighbouring U-Th dates are slightly
321 lower (0.94 mm/yr on average; see **Table 1**), highlighting the benefit of combining multiple
322 independent dating methods (e.g. layer counting and radiometric dating) in age models to increase
323 the accuracy of dates and growth rate reconstructions. Because of its distinct seasonal cyclicity, the
324 $\delta^{13}\text{C}$ cycle is used as a reference to deduce whether or not other proxies record the seasonal cycle. Mg
325 and Zn appear to track this seasonal cycle well as their periodograms contain peaks at 0.8 and 0.75
326 mm^{-1} respectively, corresponding closely to the frequency of $\delta^{13}\text{C}$. For Zn, a broader double peak is
327 observed with a main period of 1.18 mm and a smaller period of 1.02 mm. This double peak in the

328 periodogram is caused by small variations in the thickness of the annual cycles around a mean
329 thickness of 1.14 m with a lightly skewed distribution towards thinner layers (see Supp. Mat. Fig. 6).
330 The P record doesn't display any significant seasonal cycle (95% confidence) (**Fig. 4** and **Fig. 6**). For P20,
331 visible layers are thinner (mean 0.382 mm) and also the variation in thickness is larger (RSD 28.9%)
332 compared to P16 and P17 (Supp. Mat. Fig. 6). This results in broader and less well defined seasonal
333 peaks in the periodograms.

334 **5. Discussion**

335 **5.1 Seasonal cyclicity in stable isotope and trace element records**

336 A schematic overview of the observed changes in all proxies and their interpretation for the three
337 intervals is provided in **Table 1**. Assessing the exact phasing of the seasonal cycles of different trace
338 elements to $\delta^{13}\text{C}$ and the visible layering remains challenging since 1) A multitude of factors control
339 trace element variations within speleothems and 2) stable isotope ratios and the trace element
340 concentrations are not measured on the same exact sample localities. Whilst stable isotope ratios were
341 measured on microdrilled powders, trace element concentrations were measured using laser ablation.
342 These records were later carefully aligned based on microscopic observation of sample positions, but
343 due to differences in sample size and sampling density, the exact location of the analyses may not fully
344 coincide. An example of such a phase problem is the occurrence of an additional year in P16 in the
345 trace element curve compared to $\delta^{13}\text{C}$ (**Fig. 4**, between 1 and 6 mm). Another example is the decrease
346 in amplitude of trace element seasonality which takes place in P16 around 9 mm from the start of the
347 record. This change does not occur in the stable isotope record and therefore complicates the
348 comparison between records in the second part of the record. The fact that all trace element records
349 are effected and not the stable isotope records suggests that this transition highlights a methodological
350 issue, such as a difference in laser beam focus (e.g. due to a difference in polishing quality) during LA-
351 ICP-MS measurements, highlighting the importance of sample preparation for high resolution chemical
352 analyses (e.g. LA-ICP-MS and μXRF). Nevertheless, $\delta^{13}\text{C}$ minima generally occur in the DCL, suggesting
353 a similar timing (and maybe control) on the visible laminae and $\delta^{13}\text{C}$ cycles. Trace element proxies show
354 cyclicity with a similar frequency as the $\delta^{13}\text{C}$ (**Fig. 6**). This in contrast to $\delta^{18}\text{O}$, which shows less clear
355 seasonal cycles in P16 and P17.

356 **5.1.1 Zinc, yttrium and lead proxies**

357 In earlier monitoring studies carried out in the Pèrè-Noël Cave (also part of Han-sur-Less Cave system,
358 **Fig. 1**), the presence of a late autumn increase in discharge was identified (Genty and Deflandre, 1998;
359 Verheyden et al., 2008). In-situ conductivity measurements indicated an increase in mineral content

360 (ion concentrations) and/or organic matter during this autumnal increase in drip water discharge
361 (Genty and Deflandre, 1998). Measurements of the drip water discharge above the Proserpine
362 stalagmite show that in October and November, a doubling of the discharge volume occurs. This
363 increased discharge is maintained until May, when a gradual decrease is observed (Van Rampelbergh
364 et al., 2014). In the same period, Mg/Ca and Sr/Ca ratios in drip waters increase as a delayed response
365 to the intense July/August rainfalls (Verheyden et al., 2008). The timing of the elevated discharge
366 agrees with the theoretical water excess occurring above the cave (Genty and Quinif, 1996). At the
367 same time, Verheyden et al. (2008) postulate that autumn flushing brings humic and fulvic acids that
368 accumulate due to intense biological activity above the cave during spring and summer. The observed
369 seasonal cycle in Zn, Y and Pb in the intervals studied is likely caused by this annual autumn-winter
370 flushing. Variations in these trace metal concentrations within annual speleothem layers have
371 previously been attributed to the annual hydrological cycle. For instance, Borsato et al. (2007) linked
372 the peak concentrations of F, P, Cu, Zn, Br, Y and Pb to the annual increase of soil infiltration during
373 autumnal rainfall. Furthermore, it was suggested that the transport of such elements mainly occurs via
374 natural organic matter (NOM) or other forms of colloidal material. Enrichments of these soil-derived
375 elements within speleothems are believed to be associated with high drip water flow events (Fairchild
376 and Treble, 2009). Studies have shown that trace metals, such as Cu, Ni, Zn, Pb, Y and REE, are
377 predominantly transported via complexation by NOM, of which the fraction size in the karstic waters
378 ranges from nominally-dissolved to colloidal-to-particulate (Hartland et al., 2012; Wynn et al., 2014).
379 In the case of Zn and Pb, Fairchild et al. (2010) have shown that in Obir Cave (Austria) the visible and
380 ultra-violet lamination forms during autumn and is enriched in Zn, Pb and P. According to Wynn et al.
381 (2014), the correspondence of distinct Zn and Pb peaks with the autumnal laminae is compelling
382 evidence for a high-flux transport of these trace metals with NOM.

383 However, in this study no distinct annual cycle within the P record is observed (**Fig. 4** and **Fig. 6**). The
384 difference between records of P and other soil-derived elements (e.g. Zn and Y; which exhibit clear
385 seasonality) is difficult to explain. Phosphorus is considered soil derived as it originates from vegetation
386 dieback (Treble et al., 2003; Baldini et al., 2002). Therefore, P has shown similar variations as observed
387 in Zn, Y and Pb in previous studies (Borsato et al., 2007; Fairchild et al., 2010). In the Proserpine
388 speleothem, no relation between P and other soil derived trace elements is detected. This finding is in
389 agreement with minimal seasonal variability observed in $\delta^{18}\text{O}$ and δD values of cave water monitored
390 in 2012-2014 (Van Rampelbergh et al., 2014), suggesting that seasonal changes in the epikarst, linked
391 to water availability, were dominant over seasonal processes related to surface (soil) processes. If P
392 was predominantly mobilized by humic and fulvic acids, one would expect a seasonal pattern that

393 follows the autumn increase in discharge, in which these acids are supposedly enriched (as postulated
394 by Verheyden et al., 2008). However, such a pattern is absent from our data.

395 An explanation proposed by Frisia et al. (2012) is that P is not derived from soil leaching, but from other
396 sources such as phosphate minerals present in the epikarst or microbiological activity. However, no
397 data is available on the P concentrations in the host rock and no microbially induced petrographic
398 features were observed in the Proserpine speleothem, making it hard to test this hypothesis.

399 Alternatively, the lack of seasonality in P might be explained by the occurrence of snowmelt in the
400 earlier growth periods (P16 and P17). The delay of peak infiltration caused by snowmelt dilutes the
401 autumn flushing effect and explains the lack of an autumn peak in the P record. Snow melt may have
402 the so-called “piston effect” pushing older water out of the epikarst and therefore increasing the flow
403 of water to the speleothem site, causing increased seasonality in Mg and Sr. However, there is no
404 evidence of this delayed infiltration caused by snow melt in modern cave monitoring (Van
405 Rampelbergh et al., 2014), while seasonality is also absent in the P record of P20. Therefore, snowmelt
406 cannot fully explain the trace element patterns observed in the data.

407 Another alternative explanation might be that the limit of detection of P in our LA-ICP-MS data is higher
408 relative to the measured values than that of other elements of interest (e.g. Mg, Zn and Sr), causing
409 higher analytical noise on the P record compared to the other trace element records. The reason might
410 be that P measurements are sensitive to interferences in a Ca-rich matrix (such as calcium carbonate
411 in speleothems).

412 Because of the distinct signature of the seasonal cycle in Zn, the Zn peaks are used as tie-points to
413 create the annual stacks of other trace element records (**Fig. 7**), with lower concentrations occurring
414 during periods of lower discharge and vice versa. The much higher Zn and Y peaks in P16 compared to
415 P17 and P20 suggest an increased seasonality effect in discharge; therefore the accompanied annual
416 flushing of the soil above the cave appears more intense in the early 17th century. Concentrations of
417 Pb are significantly higher in P20 compared to the other periods (median of 0.37 $\mu\text{g g}^{-1}$ versus 0.14 $\mu\text{g g}^{-1}$
418 g^{-1} and 0.14 $\mu\text{g g}^{-1}$ in P16 and P17, respectively). An increase of Zn and Y in P20 similar to that in Pb is
419 not observed, suggesting that the Pb-enrichment occurs at the soil level from another source. A study
420 of Allan et al. (2015) on Pb isotope ratios in the in the same Proserpine stalagmite shows that the Pb
421 concentrations are soil derived and originate from various sources of anthropogenic atmospheric
422 pollution (coal, industrial activities, steel production and road dust). This explains well the observed
423 higher Pb concentration in P20. Allan et al. (2015) identified increases in Pb concentration during 1945-
424 1965 CE and 1975-1990 CE, which are in agreement with the observed higher Pb concentrations in this

425 study between 20-18 mm and 13-5 mm. They also concluded that this 20th century anthropogenic
426 pollution only affects Pb and none of the other elements used as palaeoseasonality proxy in this study.

427 5.1.2 Magnesium, strontium and barium proxies

428 **Figure 7** shows that the annual stacks of Sr and Ba correlate strongly within all three intervals,
429 evidenced by Pearson correlation coefficients (r) of 0.71, 0.97 and 0.82 for P20, P17 and P16,
430 respectively with p-values much smaller than 0.01 (99% confidence level; see also **Fig. 8**). Magnesium
431 displays an antiphase relationship with Sr and Ba in P16 ($r = -0.85$, $p = 1.8 \times 10^{-7}$) whereas in P20 this
432 relationship is in phase ($r = 0.64$, $p = 7.2 \times 10^{-4}$). For P17, there is no significant relationship between Mg
433 with Sr and Ba ($r = -0.13$, $p = 0.53$).

434 A strong covariation of Mg with Sr and Ba, as observed in P20, has previously been attributed to reflect
435 the presence of prior calcite precipitation (PCP) in the epikarst above the cave, caused by the
436 occurrence of drier periods (Fairchild et al., 2000), even on a seasonal scale (Johnson et al., 2006). The
437 presence of PCP during late summer (with high evapotranspiration above the cave), when strongly
438 reduced drip water discharge exists above the Proserpine stalagmite, has also been evoked to explain
439 the enriched $\delta^{13}\text{C}$ of freshly deposited calcite during the cave's summer mode (Van Rampelbergh et
440 al., 2014). Despite the difficulties of accurately correlating trace elements and stable isotope proxies,
441 there appears to be a distinct covariation between the P20 Mg and $\delta^{13}\text{C}$ record, with maxima in Mg
442 corresponding with maxima in $\delta^{13}\text{C}$, confirming the hypothesis of PCP control on these proxies. Like
443 PCP, a change in the morphology of the speleothem itself, resulting in prolonged degassing, might also
444 partly explain the correlation between $\delta^{13}\text{C}$ on the one hand and Mg and Sr on the other. Both these
445 processes are likely driven by a reduction of infiltration between the 17th and 20th century.

446 The antiphase correlation between Mg on the one hand and Sr and Ba on the other hand in P16
447 requires the involvement of other processes that dominate over PCP. A positive relationship between
448 the Mg partition coefficient and temperature would be expected from thermodynamic considerations,
449 and this has indeed been observed in experimental carbonate precipitation studies (Gascoyne, 1983;
450 Rimstidt et al., 1998; Huang and Fairchild, 2001; Day and Henderson, 2013). In similar experiments,
451 strontium partitioning into inorganic carbonate is known to remain constant with increasing
452 temperatures but can be influenced by calcite precipitation rate (Day and Henderson, 2013). Faster
453 precipitation of calcite causes an increased amount of lattice defects, resulting in an increased value
454 for the partition coefficient of Sr (Pingitore, 1978; Pingitore and Eastman, 1986; Pingitore et al., 1992)
455 and thus more Sr uptake in the calcite. Higher temperatures, combined with a decrease in drip water
456 discharge, leading to decreased growth rates, could therefore theoretically explain the antiphase
457 relationship of Mg and Sr (Huang et al., 2001). However, growth rates in P16 are rather high and

458 additionally, it has been suggested that the variations of Sr and Mg in drip water chemistry are often
459 significantly higher than those caused by the processes mentioned above (Van Beynen et al., 1997).
460 Roberts et al. (1998) concluded that the temperature-dependence of the Mg partition coefficient could
461 theoretically explain seasonal Mg variations, but not the multi-annual trends, for which hydrological
462 changes are likely more important. Such observations have caused the interpretation of the Mg proxy
463 to shift from a temperature relationship to an interpretation in terms of hydrological changes such as
464 amount of water recharge in the epikarst (Fairchild and Treble, 2009).

465 In this case, an alternative explanation for the P16 antiphase relation in Mg, Sr and Ba is the
466 incongruent dissolution of dolomite (IDD of $\text{CaMg}(\text{CO}_3)_2$), taking place during annual periods that are
467 characterized by enhanced water-rock interaction. The presence of dolomite within Givetian limestone
468 deposits overlying the cave has been recognised by Verheyden et al., (2000), Fairchild et al. (2001) and
469 Pas et al. (2016). During periods of decreased recharge, i.e. summer for the Han-sur-Lesse Cave,
470 prolonged interaction between water and rock leads to saturation of the karstic water with respect to
471 CaCO_3 . When saturation is reached, incongruent dissolution of dolomite (IDD) will start and Ca^{2+}
472 concentration remains constant due to the precipitation of calcite (Lohmann, 1988). IDD increases the
473 Mg/Ca of the drip water (Fairchild et al., 2000), but lowers the Sr/Ca and the Ba/Ca, because dolomite
474 tends to have lower Sr and Ba contents with respect to calcite (Roberts et al., 1998). During winter
475 recharge, saturation of the water in the epikarst with respect to calcite is not attained and dolomite
476 does not dissolve. The IDD process may overwhelm the PCP signal in P16 and might be responsible for
477 the observed antiphase relation. Since the host rock of the Han-sur-Lesse cave contains both dolomite
478 and shale deposits (rich in trace elements such as Mg, Sr, Ba and Y), increased host rock interaction of
479 infiltration waters may influence the trace element concentrations of drip waters (see **Fig. 1**). The
480 dominance of the interaction with dolomite or shales on the trace element budget depends on the
481 composition of the host rock and the local pathway of the infiltration water. This makes it very hard to
482 separate these different processes that influence the trace element composition of the Proserpine
483 speleothem. The fact that host rock interaction is dominant in P16 but not in P17 and P20 might
484 indicate that in the 16th century, these periods of decreased recharge of the epikarst were more
485 common, suggesting that a more seasonal precipitation or evapotranspiration regime was in place in
486 the 16th century and that seasonality in water availability (and therefore epikarst recharge) was
487 reduced in later times. Higher recharge in the 16th and 17th centuries is also evident from the thicker
488 annual laminae in P16 and P17 compared to P20, showing that the Proserpine speleothem grew faster
489 during these times, which points towards faster drip rates.

490 A third process that could cause changes in the phase relationship between Mg, Sr and Ba is a change
491 in land use, which changes soil thickness and influences the rate of infiltration of meteoric water into

492 the epikarst. Both Mg and Sr may have a twofold provenance: from soil and from host rock (Rutledge
493 et al., 2014; Belli et al., 2017). A change in land use resulting in a change in the relative contribution of
494 soil-derived dissolved ions could therefore cause the shifts in phase relationship between Mg, Sr and
495 Ba observed in **Fig. 7** and **Fig. 8**. Increased seasonal cyclicality in Y and Zn, elements associated with soil
496 activity, in P16 compared to P17 and P20 actually supports this hypothesis. The soil above the Han-sur-
497 Lesse cave is very thin (~25 cm), but its thickness might have varied through time. A change in
498 vegetation cover between the 16th century and later centuries due to, for example, changes in regional
499 climate or an increase in anthropogenic activity (e.g. forest disturbance) could have brought about
500 such a change in soil thickness above the cave and explain the changes in trace element patterns
501 observed in the Proserpine speleothem.

502 The comparison of the annual stacks for Mg, Sr and Ba of the different intervals corroborates the idea
503 that PCP is the main process controlling the seasonal variations of these trace elements in P17 and P20
504 based on the in-phase relation of Mg, Sr and Ba. Within P16, enhanced seasonality in recharge causes
505 IDD or increased concentrations of soil-derived trace elements to dominate over PCP. This is in
506 agreement with the lower $\delta^{13}\text{C}$ values for P16, indicating a higher contribution of soil CO_2 and
507 explaining the antiphase relation of Mg against Ba and Sr as a consequence of IDD. Somewhere
508 between the P16 and P17 periods, a turnover in the hydrological regime of the epikarst allowed PCP
509 to become dominant over IDD or soil contribution in the seasonal variations in the proxies. Within P17,
510 the relationship between Mg, Sr and Ba is less clear. This could point towards a change in hydrological
511 regime between the periods of deposition of P16 and P20, which was still underway during deposition
512 of the calcite in section P17 (mid-17th century).

513 **5.1.3 Uranium**

514 In speleothems, U is thought to be mainly derived from bedrock dissolution (Bourdin et al., 2011;
515 Jamieson et al., 2016) and to be subsequently transported by the ground water towards the
516 speleothem (Fairchild and Baker, 2012). The partition coefficient of U is <1 for calcite (Johnson et al.,
517 2006; Jamieson et al., 2016). This causes U to be preferentially excluded from the calcite and enriched
518 in the remaining drip water during the process of PCP. However, in P20, where PCP is evoked as the
519 dominant process controlling Mg, Sr and Ba seasonal variations, an antiphase relationship of U with
520 Mg, Sr and Ba is observed (**Fig. 7**). Johnson et al. (2006) concluded that scavenging of U as uranyl ion
521 (UO_2^{2+}) from the drip water onto the calcite crystal surfaces during PCP has a more dominant control
522 on seasonal U variability than the partition coefficient. Furthermore, the relatively fast growth rate of
523 the Proserpine speleothem limits uranyl leaching from the exposed crystal surfaces in the newly
524 formed speleothem, highlighting the dominance of epikarst processes over those taking place at the

525 speleothem surface (Drysdale et al., 2019). Such a mechanism may explain why U is antiphase with the
526 Mg, Sr and Ba variations, especially since the stalagmite is under continuous dripping of water.

527 **5.2 Seasonal variations in $\delta^{13}\text{C}$ and $\delta^{18}\text{O}$**

528 To compare and understand the seasonal variations in $\delta^{13}\text{C}$ and $\delta^{18}\text{O}$, annual stacks were created (**Fig.**
529 **9**) by resampling based on the occurrence of peaks in $\delta^{13}\text{C}$ values as this proxy reflects the seasonal
530 cycle best (**Fig. 6**). The minima in $\delta^{13}\text{C}$ always occur in DCL in P16 and P17. In P20, this relationship is
531 less clear, while most of the $\delta^{13}\text{C}$ minima do also occur within the DCL (**Fig. 4**). Van Rampelbergh et al.
532 (2014) observed seasonal changes in $\delta^{13}\text{C}$ of dripwater and recent calcite, with higher values occurring
533 in summertime when drip rates are reduced. This led them to conclude that $\delta^{13}\text{C}$ is mainly driven by
534 changes in PCP. Higher $\delta^{13}\text{C}$ values occur when more PCP is observed, i.e. during periods of lower
535 recharge. The in phase variations of Mg, Sr and Ba in P20 described above support the hypothesis of a
536 seasonally changing degree of PCP (see **Fig. 8**). Seasonal variations in the amount of PCP and its effect
537 on $\delta^{13}\text{C}$ has previously been recognized in monsoon regions (Johnson et al., 2006; Ridley et al., 2015).
538 In P16, seasonal changes in host rock interaction or soil contribution dominate the trace element
539 variations of Mg versus Sr and Ba over PCP. However, since the main source of carbon in Han-sur-Lesse
540 cave waters is the vegetation cover above the cave (Genty et al., 2001), IDD is not expected to change
541 the $\delta^{13}\text{C}$ signal. For example, a case study carried out by Oster et al. (2014) showed that an increase in
542 IDD did not affect the $\delta^{13}\text{C}$ of the speleothem significantly, despite a difference of $\sim 0.5\text{‰}$ in $\delta^{13}\text{C}$
543 between the limestone and dolomite component in the host rock. Since $\delta^{13}\text{C}$ is not affected by IDD,
544 the influence of PCP on the $\delta^{13}\text{C}$ remains observable. Increased degassing related to PCP increases $\delta^{13}\text{C}$
545 in the summer season in all growth intervals. Indeed, similar as in P20, for both P17 and P16 $\delta^{13}\text{C}$
546 minima occur within DCL, suggesting that these DCL layers in these intervals were deposited during
547 seasonal periods of increased drip water discharge.

548 Observations from cave monitoring have shown that seasonal changes in cave temperature (11°C -
549 15°C) are the main driver of $\delta^{18}\text{O}$ variations in freshly deposited calcite (-7.0‰ - -6.2‰ ; Van
550 Rampelbergh et al., 2014). The $\delta^{18}\text{O}$ periodograms show that the seasonal $\delta^{18}\text{O}$ cycle is less developed
551 compared to $\delta^{13}\text{C}$ (**Fig. 6** and Supp. Mat. Fig. 3-5). This is also expressed in the annual stacks (**Fig. 9**).
552 For P20, there is tendency towards a positive correlation of $\delta^{13}\text{C}$ and $\delta^{18}\text{O}$ but in P17 and P16 this is
553 unclear. Although analyses of recent calcite have clearly shown that $\delta^{18}\text{O}$ values are at least partly
554 controlled by the cave temperature, interpretation of the seasonal $\delta^{18}\text{O}$ changes is difficult due to the
555 reduced seasonal cyclicity in the $\delta^{18}\text{O}$ records compared to other proxies. However, mean $\delta^{18}\text{O}$ values
556 of speleothem calcite are obviously more depleted for P17 and P16 compared to P20 (**Fig. 4** and **Fig.**
557 **5**). Temperature changes over this period could in theory explain some variation in $\delta^{18}\text{O}$, but only if

558 these cooler temperatures resulted in cooler cave temperatures as well, and only if fractionation was
559 in equilibrium with ambient air, which is not certain for the 17th century part of the Proserpine. In
560 addition, this local temperature trend of $\sim 1^\circ\text{C}$ is not visible in the long-term $\delta^{18}\text{O}$ record of **Fig. 3**,
561 suggesting that other factors have a stronger influence on the oxygen isotope fractionation in this
562 speleothem (e.g. the $\delta^{18}\text{O}$ of precipitation). Therefore, the hypothesis put forward here is that the
563 lower mean $\delta^{18}\text{O}$ values of P16 point towards an increase in winter precipitation above the cave, since
564 Van Rampelbergh et al. (2014) has shown that winter precipitation, such as the presence of snow,
565 above Han-sur-Lesse cave causes a severe decrease in $\delta^{18}\text{O}$ of the precipitation. Subsequently, this
566 decrease is then transferred to the drip water and into the speleothem calcite.

567 **5.3 Variability in the seasonal cycle**

568 The observed changes of the seasonal variations in $\delta^{13}\text{C}$, Mg, Sr and Ba between P20, P17 and P16 can
569 only be explained by a change in the processes controlling the seasonal variability in $\delta^{13}\text{C}$, Mg, Sr and
570 Ba (**Fig. 9**). In the recent period, between 1960 and 2010 CE (P20), PCP is identified as the main driver
571 for seasonal changes in Mg, Sr, Ba trace element concentrations. This hypothesis is supported by the
572 $\delta^{13}\text{C}$ variations. In the 16th century, Mg, Sr and Ba variations suggest that IDD or soil activity, rather
573 than PCP, dominate the seasonal signal. Fairchild and Baker (2012) defined the term transfer function
574 to describe the quantitative relation between speleothem chemistry and changing cave environments
575 or climate. This transfer function depends on several chemical and environmental variables, whose
576 importance may change over time. In this case, there is a (qualitative) change in the transfer function
577 which causes PCP to outweigh IDD and soil activity from the 16th century to modern times. This change
578 in transfer function is likely controlled by a change in the environment around the cave (e.g. change in
579 land use or precipitation regime) since there are no indications for drastic changes in cave morphology
580 over the last 500 years, as interpreted from the long term stable isotope ratio record (**Fig. 3**; Van
581 Rampelbergh et al., 2015). As mentioned above, a likely candidate for this environmental change is a
582 change in land use (either natural or anthropogenic) between the 16th century and modern times,
583 which could strongly influence soil activity, making soil activity a much less important factor in the
584 trace element budget in the 17th and 20th century compared to the 16th century.

585 It is known that the strength of the acting transfer function can be used as a palaeoclimate proxy. For
586 example, Jamieson et al. (2016) demonstrated that the seasonal (anti-)correlation between $\delta^{13}\text{C}$ and
587 U/Ca varies through time within a Common Era stalagmite from Belize. During drier years, reduced
588 seasonal variability in prior aragonite precipitation causes U/Ca and $\delta^{13}\text{C}$ to correlate more positively
589 compared to wetter years. This illustrates how a transfer function can be regarded as a valuable
590 palaeoclimate proxy. In any case, a certain external forcing is necessary for a change in transfer

591 function to take place. A prerequisite for PCP to occur is the presence of sufficient karstic voids filled
592 with a gas phase characterized by a lower $p\text{CO}_2$ than that with which the infiltrating waters previously
593 equilibrated, or similarly lower $p\text{CO}_2$ concentrations in the cave that cause the formation of a large
594 stalagmite above the speleothem (Fairchild and Treble, 2009). The presence of such karstic voids is
595 dependent on the multi-annual to decadal recharge amount of the karstic aquifer. Indeed, the mean
596 values of trace element concentrations imply increased water availability during P16 and P17
597 compared to P20. More specifically, peaks in soil-derived trace element concentrations (Zn and Y) are
598 higher for P16, pointing towards enhanced flushing and an increased seasonality in water availability
599 as well as an increase in soil activity. This hypothesis is supported by the observation of marked
600 increases in drip rates in the cave during winter (Genty and Deflandre, 1998). An anthropogenic
601 influence explains the higher concentrations of Pb in P20, but may also partly explain the change that
602 occurs between the 16th century and later times. Sadly, no detailed information is available about the
603 local changes in land use in between the 16th and 17th centuries. However, it is inferred that forest
604 cover above the Han-sur-Lesse cave system was indeed reduced between the little ice age and modern
605 times due to increased anthropogenic activity (e.g. Van Rampelbergh et al., 2015). These changes
606 mostly occurred on the more humid slopes rather than the drier tops of the hills. Since the Salle du
607 Dôme is situated under the top of the hill (formed by the anticline structure mentioned in section 2.1),
608 changes in local forest cover are relatively small, but cannot be neglected. Lastly, layers in P16 and P17
609 are up to three times thicker compared to P20 (**Table 2, Fig. 3** and Supp. Mat. Fig. 6), which reflects
610 higher growth rates. The positive relationship between water supply and growth rate has been
611 demonstrated in the past (Baker et al., 1998; Genty and Quinif, 1996). In large and irregular shaped
612 stalagmites, such as the Proserpine, within-layer thickness can often be quite large (Baker et al., 2008).
613 The long-term layer thickness evolution shows a clear difference between the 17th century and present
614 day. The significantly thinner layers during recent times clearly indicate that less water is available
615 compared to the 17th century.

616 A straightforward explanation for the observed wetter cave conditions during, in particular, P16 is an
617 increase in seasonal water excess. Genty and Deflandre (1998) already demonstrated the strong
618 correlation between water access and drip rates in the Han-sur-Lesse cave system. Elevated water
619 excess can be caused by an increase in precipitation or a decrease in temperature. Lower
620 temperatures, especially during summer, result in a decreased evaporation of surface water.
621 Calculations of present-day potential evapotranspiration (PET) with the Thornthwaite equation
622 (Thornthwaite and Mather, 1957) for the period 1999-2012 show a negative water excess lasting from
623 May to September (**Fig. 2**). Although the Thornthwaite and Mather (1957) method does not include
624 vegetation effects, it is still a reliable tool to provide an idea of the effect of changes in the temperature

625 and/or precipitation on the PET (Black, 2007). The effect of a temperature decrease during summer
626 months on the water excess was simulated with an arbitrarily chosen 1°C temperature drop compared
627 to the 1999-2012 mean monthly temperature. Such a temperature drop appears to have only a minor
628 influence (**Fig. 2**). A hypothetical increase of total annual rainfall with 200 mm, equally spread across
629 12 months, has a much larger effect on the water excess (**Fig. 2**). However, this would decrease the
630 length of the annual interval during which no recharge occurs (i.e. only during June-July instead of
631 May-September) providing less suitable conditions for dolomite dissolution to occur. It must be noted
632 that rapid channelling of excess precipitation from intense rainfall events (especially during summer)
633 into karst voids may decrease the relevance of seasonal changes in evapotranspiration (e.g. White and
634 White, 2013). This further stresses the importance of changes in the precipitation regime on
635 seasonality in water excess. The land use change proposed above would have influenced the
636 infiltration regime. A change in forest cover since the 16th century, affecting soil thickness, would have
637 the effect of increasing seasonality in soil-derived trace elements, especially in combination with an
638 increase in precipitation seasonality. Therefore, two explanations could explain the seasonal-scale
639 variability in trace element and stable isotope composition observed in the Proserpine speleothem.
640 Firstly, a stronger seasonal distribution in the amount precipitation (with more winter precipitation)
641 could have driven an increase in host rock interaction in the 16th century, whereas today very little
642 seasonality in the amount of rainfall is observed. Secondly, a change in soil activity due to increased
643 forestation in the 16th century compared to modern times could have produced the strong seasonality
644 in soil derived trace elements in Proserpine due to seasonally enhanced leaching. The presented data
645 do not allow conclusive distinction between these two processes, and a combination of both (one
646 enhancing the other) is also possible.

647 **5.4 Implications for 17th century palaeoclimate**

648 The majority of Common Era continental palaeoclimate reconstructions are based on tree-ring data
649 (D'Arrigo et al., 2006), although other records, for example historical documents (e.g., Dobrovlny et
650 al., 2010), ice cores (e.g., Zennaro et al., 2014) or speleothems (e.g., Baker et al., 2011; Cui et al., 2012)
651 are used as well. Over the last decades, consensus has been reached that changes in solar irradiance
652 and volcanic activity are the main drivers of short-term (decadal to centennial) natural climate
653 variability during the last millennium (e.g. Crowley, 2000; Bauer et al., 2003). Interpretations of the
654 stable isotope and trace element proxies obtained on the Proserpine speleothem as well as the
655 increased thickness of annual laminae show that a higher recharge state of the karstic aquifer
656 characterizes the 17th century intervals compared to 1960-2010. Such an increase in recharge requires
657 a decrease in evapotranspiration, which can result either from lower summer temperatures or higher
658 total annual precipitation. Although it is difficult to discriminate between both, the effect of a total

659 annual precipitation increase on the recharge is expected to be higher compared to a decrease in
660 summer temperature (**Fig. 2**). As mentioned above, a change in land cover (both from anthropogenic
661 or natural causes) could also have played a role by locally affecting the infiltration of this excess
662 precipitation. Globally dispersed regional temperature reconstructions indicate that multi-decadal
663 warm or cold intervals, such as the Medieval Warm Period or the Little Ice Age (LIA), are not global
664 events. Yet, a global cooling trend starting at 1580 CE is observed in the majority of the reconstructions
665 (PAGES 2k Consortium, 2013). Several palaeoclimate reconstructions agreed upon the occurrence of a
666 cold period around 1600 CE, with negative temperature anomalies persisting in Europe at decadal and
667 multi-decadal scales (Ljungqvist et al., 2012; Luterbacher et al., 2016; Masson-Delmotte et al., 2013).
668 Reconstructions of European summer temperature provided by Luterbacher et al. (2016) indicate that
669 the coldest 11 and 51 year period since 755 CE in the area of Han-sur-Lesse cave occurred within the
670 17th century. These reconstructions showed a summer temperature decrease of 1 – 1.5°C around 1600-
671 1650 CE. Although the 17th century has been recognized as the coldest of the past twelve centuries,
672 hydrological climate conditions appear close to the long-term mean (Ljungqvist et al., 2016), with no
673 significant wetting or drying trend. However, to account for the differences between the 1960-2010
674 interval and the 17th century observed in this study, an increase in the amount winter precipitation is
675 needed, suggesting that climatic conditions were wetter during that time. Such a hypothesis is also
676 supported by the depleted $\delta^{18}\text{O}$ values in P16, indicating an increase in winter precipitation.

677 **5.5 Implications for speleothem palaeoclimate studies**

678 This study complements a longer speleothem stable isotope compositional time series with shorter,
679 higher resolution stable isotope and trace element records which capture changes on a sub-annual
680 scale. One of the major advantages of this approach is the ability to study phase relationships between
681 proxies at the seasonal level. The seasonal cycle is the strongest cycle in Earth's climate, and therefore
682 allows relationships between speleothem proxy records to be tested in a context that is more familiar
683 than that of decadal to millennial oscillations, which are less well understood. Comparing the seasonal
684 expression of speleothem proxies also allows more straightforward comparison of proxy records with
685 cave monitoring time series, which typically run on seasonal time scales (see Van Rangelbergh et al.,
686 2014). The high-resolution analyses carried out within the context of this study are relatively labour
687 intensive. Measurements at this resolution are thus likely not feasible along the full (centuries- to
688 millennia-long) growth period of a speleothem, even if seasonal variability is consistently recorded for
689 the entire growth duration. Instead, we propose that the application of high-resolution, multi-proxy
690 transects placed on strategic places along the growth axis of a speleothem (e.g. those parts where
691 seasonal lamination is particularly well expressed) may be used to provide “snapshots” of seasonal
692 proxy variability superimposed on longer term (decadal to millennial scale) variability in the record.

693 This exercise teaches us that the expression of trace element records should not be seen as a result of
694 a constant transfer function, but rather as a complex interplay between chemical, speleological and
695 environmental variables whose influence on the chemistry and (micro)morphology of the speleothem
696 changes over time. Such changes in the transfer function have implications for the interpretation of
697 the longer, lower resolution proxy records. This study therefore highlights the importance of including
698 multiple proxies (e.g. trace element in combination with stable isotope, sedimentary and/or
699 crystallographic analyses) as well as multiple sampling densities (high- and low resolution sampling) to
700 reliably interpret speleothem archives in terms of climate and environmental evolution.

701

702 **6. Conclusions**

703 This study of annual trace element and stable isotope ($\delta^{13}\text{C}$ and $\delta^{18}\text{O}$) variations over three different
704 time intervals of the annually laminated Proserpine stalagmite from the Han-sur-Lesse Cave (Belgium)
705 shows that seasonal changes in Mg, Sr and Ba during the recent period (1960-2010) suggest a strong
706 effect of prior calcite precipitation, caused by lower water availability during summer. In the 17th
707 century (1600 CE \pm 30 and 1640 CE \pm 30), however, Mg is in antiphase with Sr and Ba. This implies that
708 another process overwrites the PCP dominated seasonal cycle in these trace elements. A varying
709 degree of incongruent dolomite dissolution, with more dissolution occurring during summer when
710 water residence times in the epikarst are longer, or a more dominant influence of soil activity on the
711 trace element budget due to changes in land use are plausible hypotheses. The transfer function
712 governing the trace elements concentrations in the Proserpine speleothem is driven over the last
713 centuries by changing contributions of PCP, dolomite dissolution and soil leaching. Stable isotope
714 ratios ($\delta^{13}\text{C}$ and $\delta^{18}\text{O}$), soil derived trace element concentrations (Zn, Y and Pb) and speleothem
715 morphology indicate that the multi-annual recharge of the epikarst was higher in the 17th century. The
716 change in the response of Mg, Sr and Ba in the Proserpine speleothem to environmental changes was
717 identified to be driven by climate or by changes in land use. It may result from an increase in recharge
718 caused by a combination of lower summer temperatures and an increase in the amount of winter
719 precipitation in the 17th century for the Han-sur-Lesse cave region, or by a change in the vegetation
720 cover between the 16th and 17th century, which reduced the importance of soil processes on trace
721 element compositions in the cave's drip waters. The effect of an increase in winter annual precipitation
722 on the recharge is expected to be larger compared to a decrease in summer temperature. The data
723 obtained in this study therefore point towards a stronger seasonal cycle in cave hydrology during the
724 17th century.

725 This high-resolution, multi proxy study provides a good example of how the relative importance of
 726 different processes on trace element concentrations in speleothem calcite can change over time. This
 727 observation has implications for future speleothem-based palaeoclimate reconstructions, since
 728 transfer functions for specific cave sites, determined by cave monitoring, are often assumed to remain
 729 constant when no drastic changes in the cave environment have occurred. As the change in trace
 730 element proxy transfer function observed in this study is driven by environmental change, this change
 731 by itself can serve as a valuable palaeoclimate proxy.

732 **Author contributions**

733 Stef Vansteenberge and Sophie Verheyden designed the study. Stef Vansteenberge, Steven Goderis
 734 and Stijn Van Malderen carried out LA-ICP-MS measurements. Stef Vansteenberge, Matthias Sinnesael
 735 and Niels de Winter carried out stable isotope measurements. Stef Vansteenberge carried out the data
 736 processing and plotting with contributions from Steven Goderis, Niels de Winter and Matthias
 737 Sinnesael. Frank Vanhaecke and Philippe Claeys provided laboratory facilities and supported the
 738 measurements. Stef Vansteenberge, Niels de Winter and Matthias Sinnesael prepared the manuscript
 739 with contributions from all co-authors. Niels de Winter, Matthias Sinnesael and Sophie Verheyden
 740 revised the manuscript in response to review comments.

741 **Acknowledgements**

742 The authors would like to thank dr. Robert Andrew Jamieson and two anonymous reviewers for their
 743 thoughtful comments on the first version of this manuscript, as well as handling editor dr. James
 744 Thornalley for moderating the review process. All authors thank the Domaine des Grottes de Han
 745 S.A. for allowing us to sample the stalagmites and carry out other fieldwork. Special thanks for M.
 746 Van Rampelbergh, whose PhD research formed the base of this study. S. Vansteenberge thanks J.
 747 Van Opdenbosch and A. Ndirembako for their help collecting the stable isotope data and D.
 748 Verstraeten for the lab assistance. This research was funded by the VUB Strategic Research Funding
 749 (S. Vansteenberge), FWO Flanders (M. Sinnesael and S. Goderis), IWT Flanders (N. J. de Winter),
 750 Research grant G017217N (S. J. M. Van Malderen and F. Vanhaecke) and the Hercules Foundation
 751 (upgrade of the VUB Stable Isotope Laboratory).

752 **Table 1**

Proxy	P20	P17	P16
Mean Layer Thickness and growth rate	Thin: 0.382 mm Larger variations (RSD = 28.9%) U-Th mean growth rate: 0.564 mm/yr	Thick: 1.096 mm Smaller variations (RSD = 6.3%) U-Th mean growth rate: 1.34 mm/yr	Thick: 1.135 mm Smaller variations (RSD = 9.5%) U-Th mean growth rate: 0.910 mm/yr

$\delta^{18}\text{O}$	Strong seasonality: tendency towards in phase correlation with $\delta^{13}\text{C}$ Partially T-controlled, but other processes as well	Weak to no seasonality: unclear relation with $\delta^{13}\text{C}$	Weak to no seasonality: unclear relation with $\delta^{13}\text{C}$
$\delta^{13}\text{C}$	Clear $\delta^{13}\text{C}$ cycle: Low $\delta^{13}\text{C}$ mostly in DCL but not always $\delta^{13}\text{C}$ driven by seasonal changes in PCP	Clear $\delta^{13}\text{C}$ cycle: Low $\delta^{13}\text{C}$ always in DCL $\delta^{13}\text{C}$ driven by seasonal changes in PCP	Clear $\delta^{13}\text{C}$ cycle: Low $\delta^{13}\text{C}$ always in DCL $\delta^{13}\text{C}$ driven by seasonal changes in PCP
Mg and Sr - Ba	Good in phase correlation Mg, Sr and Ba driven by seasonal changes in PCP	Phase relation not clear Transition period between P16 and P20 hydrological regimes	Anti-phase correlation between Mg and Sr, Ba Seasonally occurring IDD dominates over PCP
Zn, Y and Pb	Weak seasonality in Zn and Y, Strong seasonality in Pb Decreased flushing, anthropogenic Pb enrichment	Weak seasonality in Zn, Y and Pb Decreased flushing	Very strong seasonality in Zn and Y, weak seasonality in Pb Enhanced flushing
U	Strong seasonality, antiphase with Mg, Sr and Ba No PCP control, scavenging	Weak seasonality antiphase with Sr and Ba scavenging	No seasonality
Remarks	Link with trace elements and layering is challenging	Link with trace elements and layering is challenging	Link with trace elements and layering is challenging

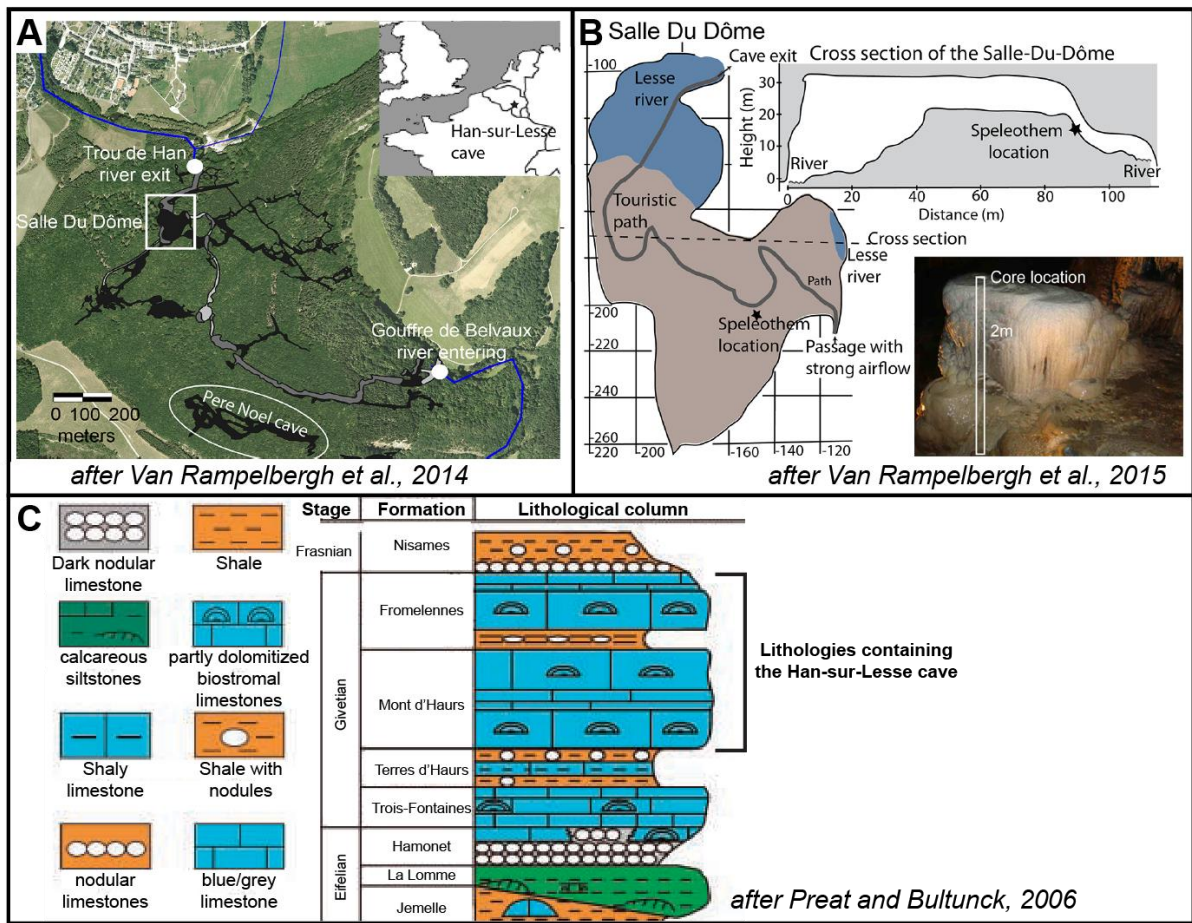
753 **Table 1: Schematic overview providing the observed changes and interpretation for the different**
754 **proxies of P20, P17 and P16. PCP = prior calcite precipitation, IDD = incongruent dissolution of**
755 **dolomite, DCL = dark compact layers, WPL = white porous layers**

756

757

Isotope	²⁵ Mg	²⁷ Al	²⁹ Si	³¹ P	³⁴ S	³⁹ K	⁵⁵ Mn	⁵⁷ Fe
LOD (µg g ⁻¹)	4.0	9.0	100	1.0	7.0	7.0	0.08	4.0 ⁷⁵⁸
Isotope	⁶⁶ Zn	⁸⁵ Rb	⁸⁸ Sr	⁸⁹ Y	¹³⁷ Ba	²⁰⁸ Pb	²³² Th	²³⁸ U ⁷⁵⁹
LOD (µg g ⁻¹)	0.2	0.03	0.08	0.01	0.1	0.008	0.0005	0.0001 ⁷⁶⁰

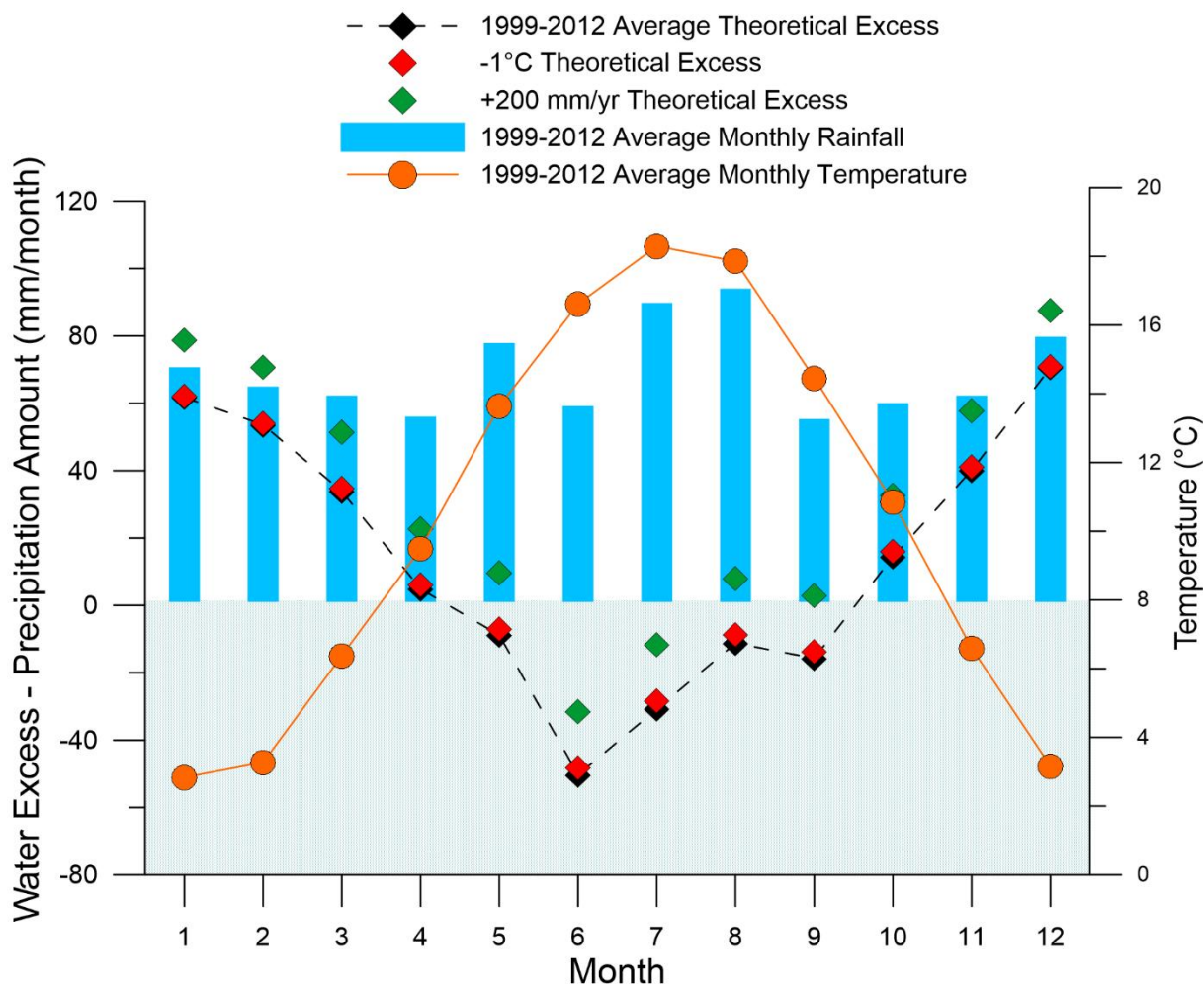
761 **Table 2:** Overview of limits of detection (LOD) of trace elements measured for this study using LA-ICP-
 762 MS.



764

765 **Figure 1:** (A) Location of the Han-sur-Lesse Cave system (50°06'51"N, 5°12'12"E) with the entrance and
 766 exit of the Lesse River, the Salle-du-dome and the Père-Noël Cave. North is upwards (B) Map showing
 767 the location of the Proserpine stalagmite within the Salle-du-Dôme. The insert shows the position of
 768 the core retrieved from the speleothem. Images adapted from Van Rampelbergh et al. (2014, 2015).
 769 (C) Lithological column of the Devonian strata in the Synclinorium of Dinant including the two
 770 formations (Fromellennes and Mont d'Hours) in which the Han-sur-Lesse cave is situated. Note the

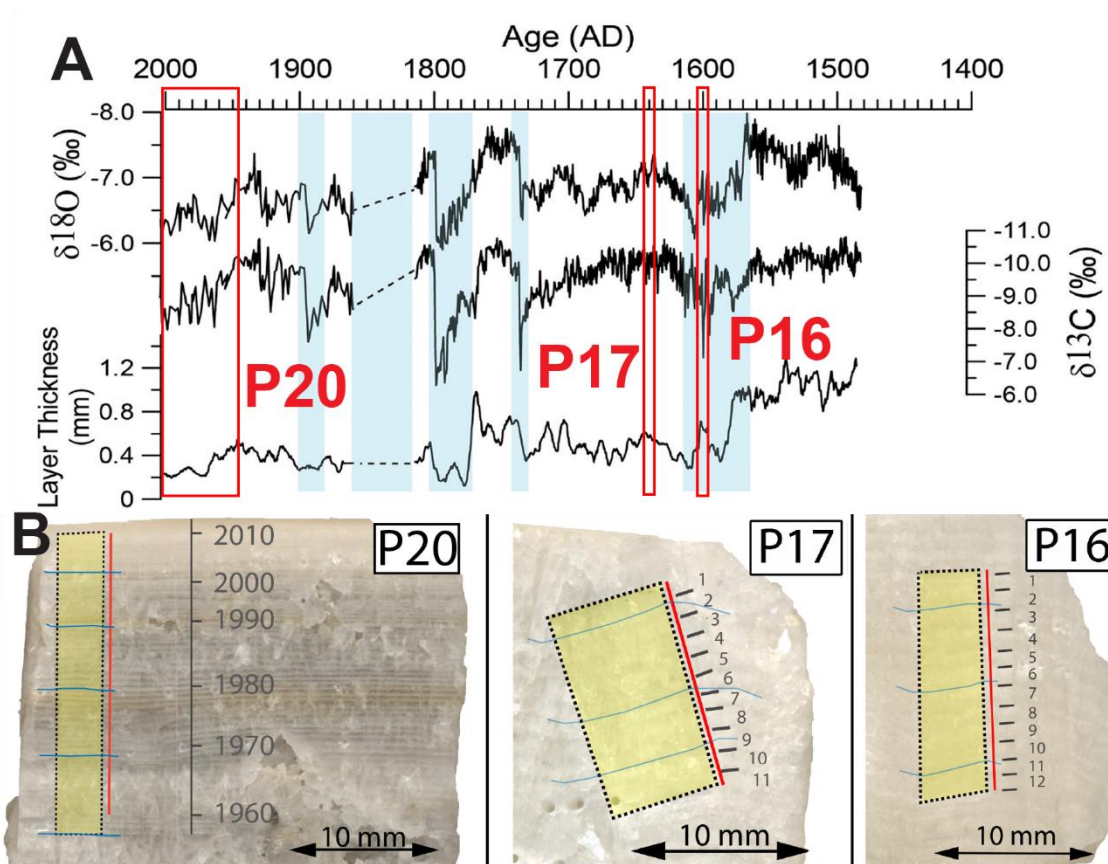
771 presence of partly dolomitized biostromal limestones and shales in both these formations.



772

773 **Figure 2:** Chart showing the calculated theoretical amount of water excess calculated with the
774 Thornthwaite equation (Thornthwaite and Mather, 1957), based on temperature and precipitation
775 data near Han-sur-Lesse cave from 1999 to 2012 (Royal Meteorological Institute, KMI). X-axis
776 represents the months from January (1) to December (12).

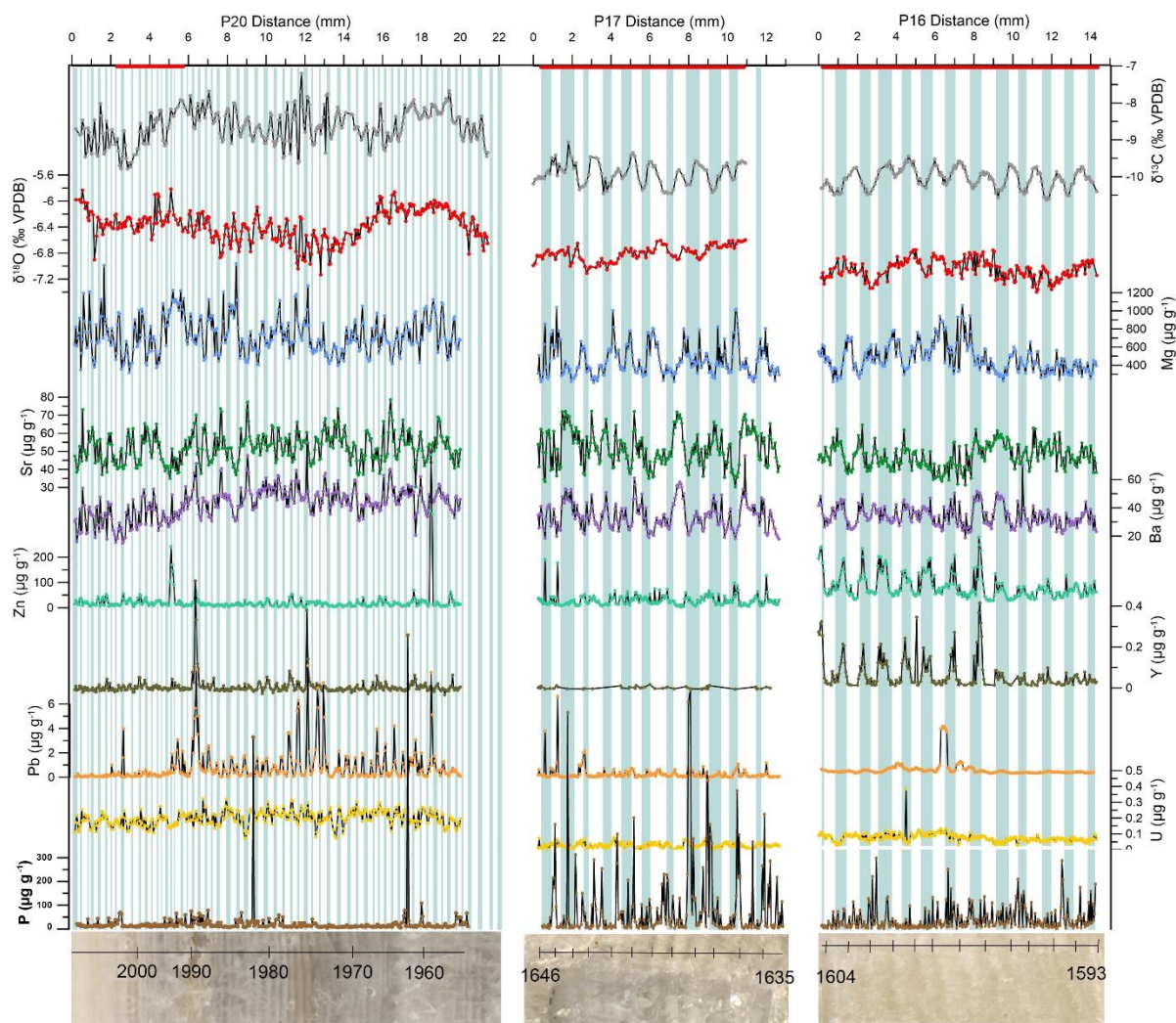
777



778

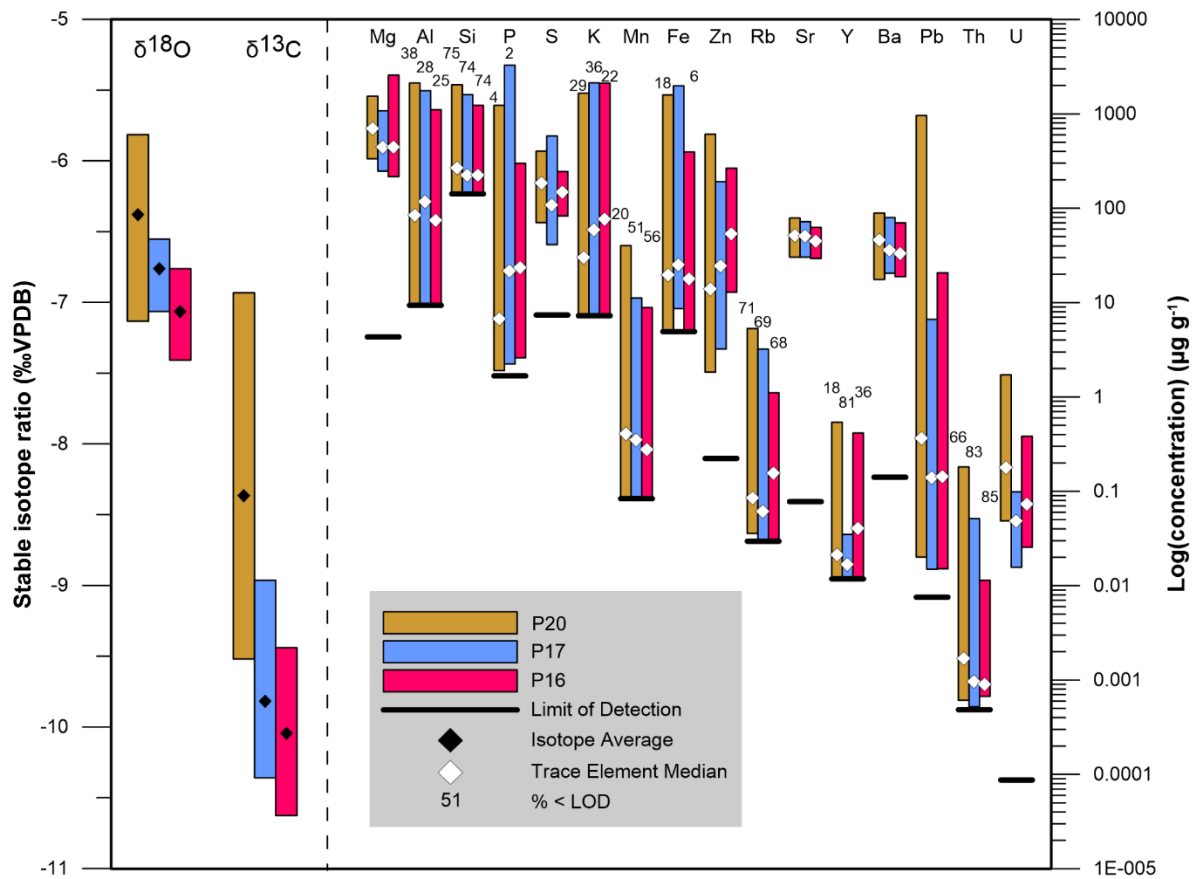
779 **Figure 3:** A. Overview of long (~500 yr) record of stable isotope ratios and annual layer thickness
 780 through the Proserpine speleothem measured by Van Rangelbergh et al. (2015). Red boxes indicate
 781 the locations of high-resolution transects discussed in this study. B. The three studied growth periods
 782 P20 (1960-2010 CE), P17 (1633-1644 ± 30 CE) and P16 (1593-1605 ± 30 CE). The yellow rectangles mark
 783 the sections that were drilled/sampled for $\delta^{13}\text{C}$ and $\delta^{18}\text{O}$ analysis, the red lines represent the LA-ICP-
 784 MS transects. Numbers in grey indicate the observed layer couplets. Note that the images (B) of parts
 785 of the Proserpine speleothem that contain the three growth periods are oriented vertically (top of the
 786 picture upwards), but that the transects themselves are oriented parallel to the local growth direction
 787 (perpendicular to the growth laminae marked in blue). This results in transect P17's orientation at a

788 $\sim 25^\circ$ angle with respect to the image (and the vertical).



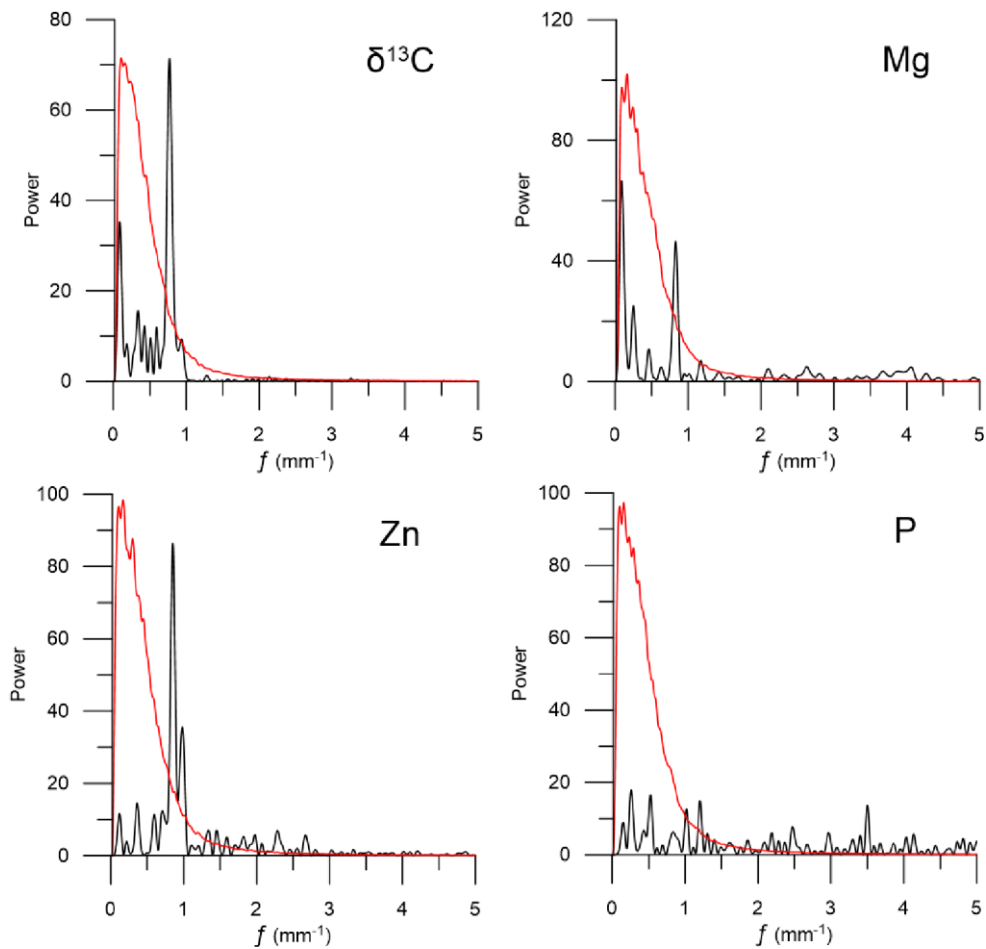
789

790 **Figure 4:** Stable isotope ratios and trace element variations plotted against distance for P20, P17 and
791 P16. Blue bars mark the DCC laminae. The left side represents the youngest layers. All stable isotope
792 ratios are expressed as ‰ VPDB, while trace element concentrations are reported in ppm. Red bars
793 indicate years used for annual stack (**Fig. 7 and 9**).



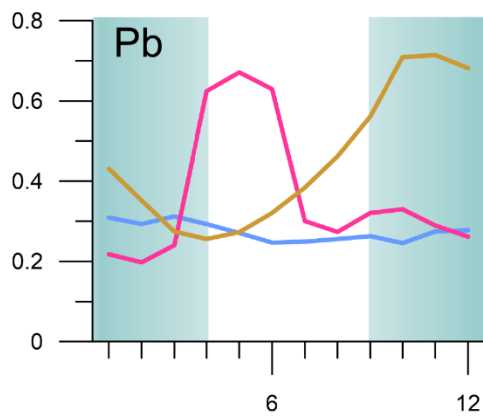
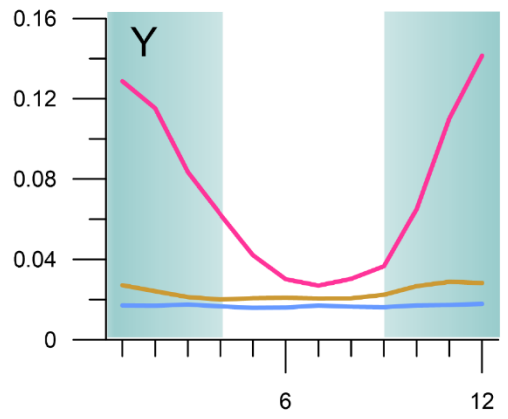
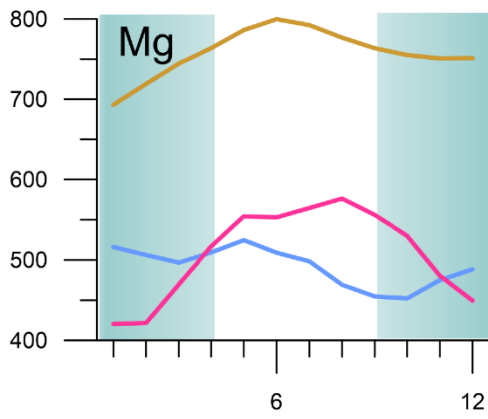
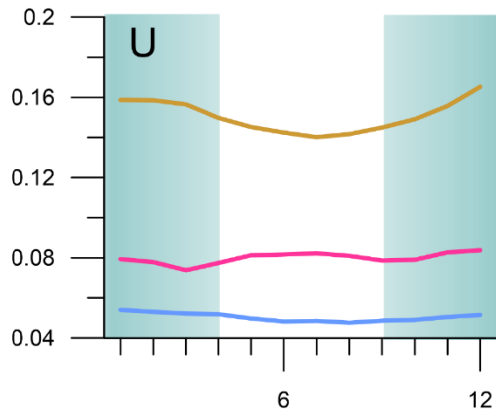
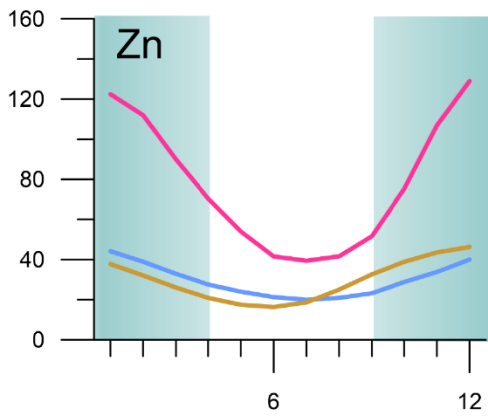
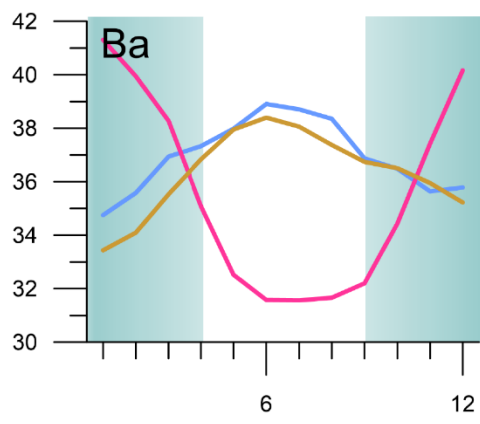
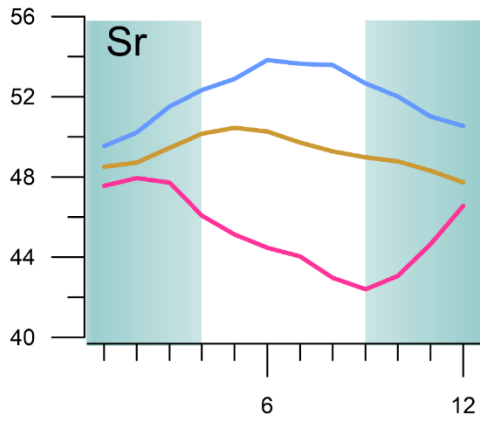
794

795 **Figure 5:** Ranges of the stable isotope (left) and trace element data (right). For the stable isotope
 796 ratios, the data mark the mean (diamonds) and the standard deviation (1σ) of the distribution. For
 797 the trace element concentrations, the boxes represent the minimum and maximum values and the
 798 white diamonds mark the median. Numbers on top of the bars represent the percentage of the data
 799 that is below the calculated detection limit.



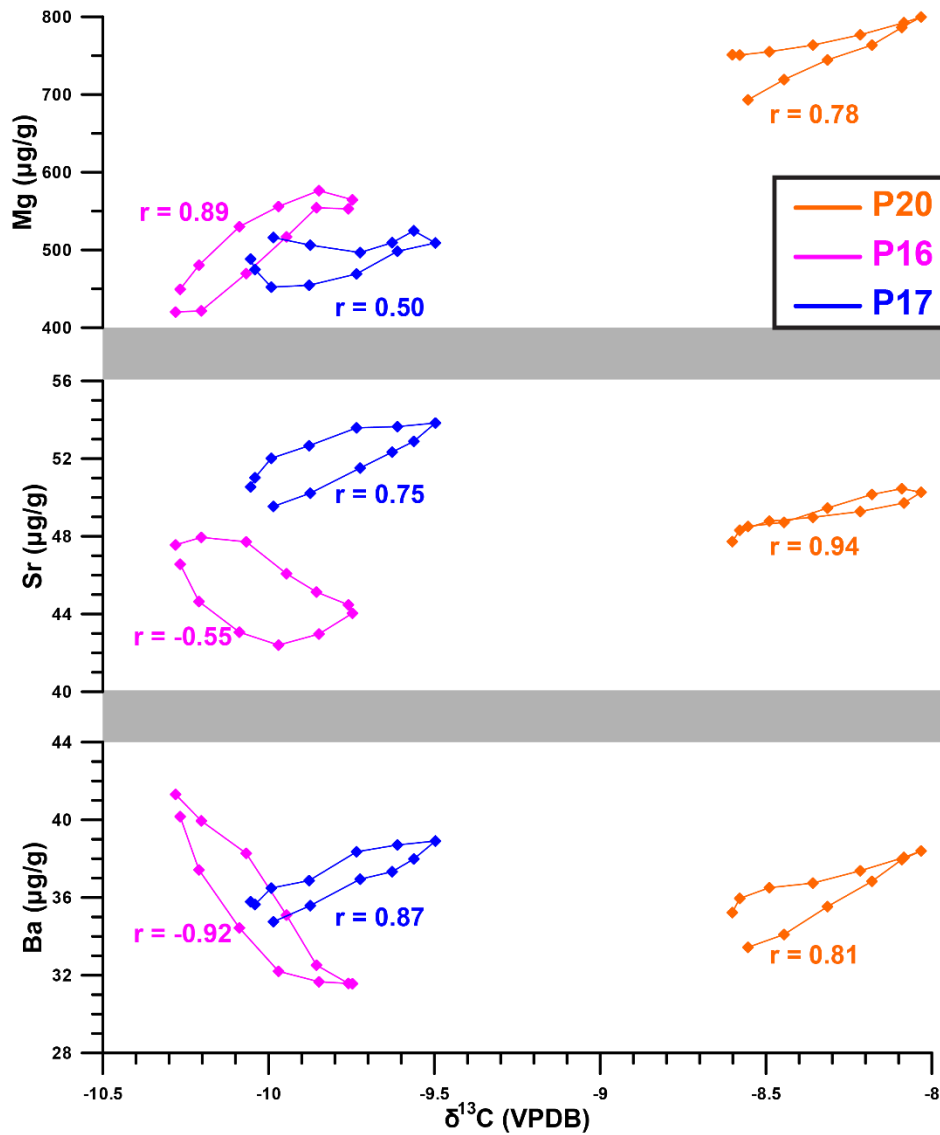
800

801 **Figure 6:** Periodograms (FFT) of $\delta^{13}\text{C}$, Mg, Zn and P measured in P16 to illustrate how the quality of a
 802 proxy to record the seasonal cycle can be studied. The red line represents the 95% confidence level.
 803 $\delta^{13}\text{C}$ is taken as a reference. The periodograms include two examples of proxies with a distinct peak in
 804 the seasonal frequency band of 0.8 mm^{-1} (Mg and Zn) and one proxy with no peak (P) in the seasonal
 805 frequency band. Periodograms for all periods are provided in the supplementary material.



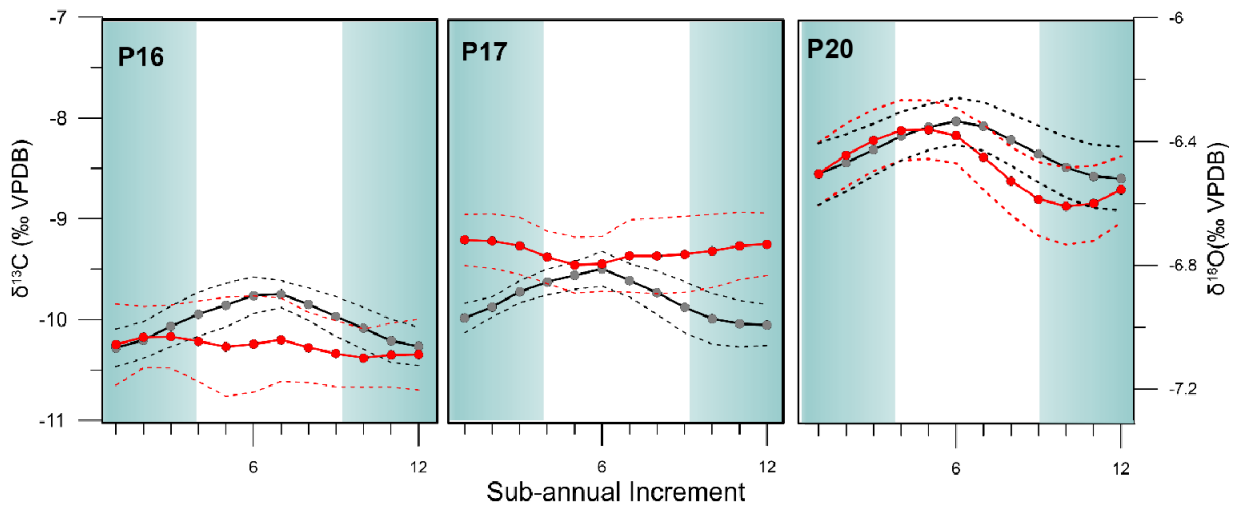
807 **Figure 7:** Annual stacks of the trace element proxies. Y-axis: concentrations ($\mu\text{g g}^{-1}$); x-axis: sub-annual
808 increment (1 = January, 12 = December). Blue shaded areas indicate the winter season. For the years
809 used, see Fig. 4.

810



811

812 **Figure 8:** Cross plot showing the relationship between monthly average trace element (Mg, Sr, Ba)
 813 concentrations and $\delta^{13}\text{C}$ values in the three growth periods. Plots are labelled with the Pearson's r
 814 values indicating the strength and direction (phase relationship) of the correlation between the
 815 variables. Note the change in phase relationship between $\delta^{13}\text{C}$ and Sr and Ba, while $\delta^{13}\text{C}$ and Mg remain
 816 positively correlated.



817

818 **Figure 9:** Annual stacks of $\delta^{13}\text{C}$ (black) and $\delta^{18}\text{O}$ (red). Dashed lines mark the 2σ uncertainty. The x-
 819 axis represents one year. Blue shaded areas indicate the winter season. For the years used, see Fig. 4.

820 **References**

- 821 Allan, M., Fagel, N., Van Rangelbergh, M., Baldini, J., Riotte, J., Cheng, H., Edwards, R.L., Gillikin, D.,
822 Quinif, Y., Verheyden, S., 2015. Lead concentrations and isotope ratios in speleothems as proxies
823 for atmospheric metal pollution since the industrial revolution. *Chem. Geol.* 401, 140-150.
- 824 Baker, A., Genty, D., Dreybrodt, W., Barnes, W.L., Mockler, N.J., Grapes, J., 1998. Testing theoretically
825 predicted stalagmite growth rate with Recent annually laminated samples: Implications for past
826 stalagmite deposition. *Geochim. Cosmochim. Acta* 62, 393-404.
- 827 Baker, A., Smith, C.L., Jex, C., Fairchild, I.J., Genty, D., Fuller, L., 2008. Annually Laminated Speleothems:
828 a Review. *Int. J. Speleol.* 37, 193-206.
- 829 Baker, A., Wilson, R., Fairchild, I.J., Franke, J., Spötl, C., Matthey, D., Trouet, V., Fuller, L., 2011. High
830 resolution $\delta^{18}\text{O}$ and $\delta^{13}\text{C}$ records from an annually laminated Scottish stalagmite and relationship
831 with last millennium climate. *Glob. Planet. Change* 79, 303-311.
- 832 Baldini, J.U.L., McDermott, F., Fairchild, I.J., 2002. Structure of the 8200-year cold event revealed by a
833 speleothem trace element record. *Science* 296, 2203-2206.
- 834 Bauer, E., Claussen, M., Brovkin, V., Huenerbein, A., 2003. Assessing climate forcings of the Earth
835 system for the past millennium. *Geophys. Res. Lett.* 30, 1276-1282.
- 836 Belli, R., Borsato, A., Frisia, S., Drysdale, R., Maas, R., Greig, A., 2017. Investigating the hydrological
837 significance of stalagmite geochemistry (Mg, Sr) using Sr isotope and particulate element records
838 across the Late Glacial-to-Holocene transition. *Geochimica et Cosmochimica Acta* 199, 247–263.
839 <https://doi.org/10.1016/j.gca.2016.10.024>
- 840 Bice, D., Montanari, A., Vucetic, V., Vucetic, M., 2012. The influence of regional and global climatic
841 oscillations on Croatian climate. *Int. J. Climatol.* 32, 1537-1557.
- 842 Black, P.E., 2007. Revisiting the Thornthwaite and Mather water balance. *J. Am. Water Resour. Assoc.*
843 43, 1604-1605.
- 844 Boch, R., Spötl, C., 2008. The origin of lamination in stalagmites from Katerloch Cave, Austria: Towards
845 a seasonality proxy. *PAGES news* 16, 1–22.
- 846 Boch, R., Spötl, C., Kramers, J.H., 2010. Early Holocene rapid climate changes recorded in fast-growing
847 stalagmites of the Alps, in: *DEUQUA-Zweijahrestagung Der Deutschen Quartärvereinigung 2010*.
- 848 Borsato, A., Frisia, S., Fairchild, I.J., Somogyi, A., Susini, J., 2007. Trace element distribution in annual
849 stalagmite laminae mapped by micrometer-resolution X-ray fluorescence: Implications for
850 incorporation of environmentally significant species. *Geochim. Cosmochim. Acta* 71, 1494-1512.
- 851 Bourdin, C., Douville, E., Genty, D., 2011. Alkaline-earth metal and rare-earth element incorporation
852 control by ionic radius and growth rate on a stalagmite from the Chauvet Cave, Southeastern
853 France. *Chem. Geol.* 290, 1-11.

854 Crowley, T.J., 2000. Causes of Climate Change Over the Past 1000 Years. *Science* 289, 270.

855 Cui, Y.F., Wang, Y.J., Cheng, H., Zhao, K., Kong, X.G., 2012. Isotopic and lithologic variations of one
856 precisely-dated stalagmite across the Medieval/LIA period from Heilong Cave, central China. *Clim.*
857 *Past* 8, 1541-1550.

858 D'Arrigo, R., Wilson, R., Jacoby, G., 2006. On the long-term context for late twentieth century warming.
859 *J. Geophys. Res. Atmos.* 111, 12.

860 Day, C.C., Henderson, G.M., 2013. Controls on trace-element partitioning in cave-analogue calcite.
861 *Geochim. Cosmochim. Acta* 120, 612-627.

862 Delvaux de Fenffe, D., 1985. Geologie et tectonique du parc de Lesse et Lomme au bord sud du
863 bassin de Dinant (Rochefort, Belgique). *Bulletin de la Société Blegé de Géologie* 94:1, 81-95.

864 de Winter, N.J., Goderis, S., Dehairs, F., Jagt, J.W., Fraaije, R.H., Van Malderen, S.J., Vanhaecke, F.,
865 Claeys, P., 2017. Tropical seasonality in the late Campanian (late Cretaceous): Comparison
866 between multiproxy records from three bivalve taxa from Oman. *Palaeogeography,*
867 *Palaeoclimatology, Palaeoecology* 485, 740–760.

868 de Winter, N.J., Vellekoop, J., Vorrsselmans, R., Golreihan, A., Soete, J., Petersen, S.V., Meyer, K.W.,
869 Casadio, S., Speijer, R.P., Claeys, P., 2018. An assessment of latest Cretaceous Pycnodonte
870 vesicularis (Lamarck, 1806) shells as records for palaeoseasonality: a multi-proxy investigation.
871 *Climate of the Past* 14, 725–749.

872 Dobrovolny, P., Moberg, A., Brazdil, R., Pfister, C., Glaser, R., Wilson, R., van Engelen, A., Limanowka,
873 D., Kiss, A., Halickova, M., Mackova, J., Riemann, D., Luterbacher, J., Bohm, R., 2010. Monthly,
874 seasonal and annual temperature reconstructions for Central Europe derived from documentary
875 evidence and instrumental records since AD 1500. *Clim. Change* 101, 69-107.

876 Dreybrodt W., 1999. Chemical kinetics, speleothem growth and climate. *Boreas* 28:347-356.

877 Drysdale, R.N., Zanchetta, G., Baneschi, I., Guidi, M., Isola, I., Couchoud, I., Piccini, L., Greig, A., Wong,
878 H., Woodhead, J.D., Regattieri, E., Corrick, E., Paul, B., Spötl, C., Denson, E., Gordon, J., Jaillet, S.,
879 Dux, F., Hellstrom, J.C., 2019. Partitioning of Mg, Sr, Ba and U into a subaqueous calcite speleothem.
880 *Geochimica et Cosmochimica Acta* 264, 67–91.

881 Fairchild, I.J., Borsato, A., Tooth, A.F., Frisia, S., Hawkesworth, C.J., Huang, Y.M., McDermott, F., Spiro,
882 B., 2000. Controls on trace element (Sr-Mg) compositions of carbonate cave waters: implications
883 for speleothem climatic records. *Chem. Geol* 166, 255-269.

884 Fairchild, I.J., Baker, A., Borsato, A., Frisia, S., Hinton, R.W., McDermott, F., Tooth, A.F., 2001. Annual
885 to sub-annual resolution of multiple trace-element trends in speleothems. *J. Geol. Soc. London* 158,
886 831-841.

887 Fairchild, I.J., Spötl, C., Frisia, S., Borsato, A., Susini, J., Wynn, P.M., Cauzid, J., Eimf, 2010. Petrology and
888 geochemistry of annually laminated stalagmites from an Alpine cave (Obir, Austria): seasonal cave
889 physiology. *Geol. Soc. London, Special Publications* 336, 295-321.

890 Fairchild, I.J., Treble, P.C., 2009. Trace elements in speleothems as recorders of environmental change.
891 *Quat. Sci. Rev.* 28, 449-468.

892 Friedman, I., O'Neil, J., Cebula, G., 1982. Two New Carbonate Stable-Isotope Standards. *Geostandards*
893 *Newsletter* 6, 11-12.

894 Frisia, S., Borsato, A., Preto, N., McDermott, F., 2003. Late Holocene annual growth in three Alpine
895 stalagmites records the influence of solar activity and the North Atlantic Oscillation on winter
896 climate. *Earth and Planetary Science Letters* 216, 411–424.

897 Frisia, S., Borsato, A., Fairchild, I.J., Susini, J., 2005. Variations in atmospheric sulphate recorded in
898 stalagmites by synchrotron micro-XRF and XANES analyses. *Earth and Planetary Science Letters* 235,
899 729–740. <https://doi.org/10.1016/j.epsl.2005.03.026>

900 Frisia, S., Borsato, A., Drysdale, R.N., Paul, B., Greig, A., Cotte, M., 2012. A re-evaluation of the
901 palaeoclimatic significance of phosphorus variability in speleothems revealed by high-resolution
902 synchrotron micro XRF mapping. *Clim. Past* 8, 2039-2051.

903 Gascoyne, M., 1983. Trace-element partition-coefficients in the calcite water-system and their
904 paleoclimatic significance in cave studies. *J. Hydrol.* 61, 213-222.

905 Genty, D., Baker, A., Massault, M., Proctor, C., Gilmour, M., Pons-Branchu, E., Hamelin, B., 2001. Dead
906 carbon in stalagmites: Carbonate bedrock paleodissolution vs. ageing of soil organic matter.
907 Implications for C-13 variations in speleothems. *Geochim. Cosmochim. Acta* 65, 3443-3457.

908 Genty, D., Blamart, D., Ouahdi, R., Gilmour, M., Baker, A., Jouzel, J., Van-Exter, S., 2003. Precise dating
909 of Dansgaard-Oeschger climate oscillations in western Europe from stalagmite data. *Nature* 421,
910 833-837.

911 Genty, D., Deflandre, G., 1998. Drip flow variations under a stalactite of the Pere Noel cave (Belgium).
912 Evidence of seasonal variations and air pressure constraints. *J. Hydrol.* 211, 208-232.

913 Genty, D., Quinif, Y., 1996. Annually laminated sequences in the internal structure of some Belgian
914 stalagmites - Importance for paleoclimatology. *J. Sediment. Res.* 66, 275-288.

915 Gimeno, L., Drumond, A., Nieto, R., Trigo, R.M., Stohl, A., 2010. On the origin of continental
916 precipitation. *Geophys. Res. Lett.* 37, L13804.

917 Griffiths, M.L., Drysdale, R.N., Gagan, M.K., Frisia, S., Zhao, J., Ayliffe, L.K., Hantoro, W.S., Hellstrom,
918 J.C., Fischer, M.J., Feng, Y.-X., 2010. Evidence for Holocene changes in Australian–Indonesian
919 monsoon rainfall from stalagmite trace element and stable isotope ratios. *Earth and Planetary*
920 *Science Letters* 292, 27–38.

921 Hartland, A., Fairchild, I.J., Lead, J.R., Borsato, A., Baker, A., Frisia, S., Baalousha, M., 2012. From soil to
922 cave: Transport of trace metals by natural organic matter in karst dripwaters. *Chem. Geol.* 304, 68-
923 82.

924 Huang Y., Fairchild I.J., Borsato A., Frisia S., Cassidy N.J., McDermott F., Hawkesworth C.J., 2001.
925 Seasonal variations in Sr, Mg and P in modern speleothems (Grotta di Ernesto, Italy). *Chemical*
926 *Geology* 175: 429-448.

927 Huang, Y.M., Fairchild, I.J., 2001. Partitioning of Sr²⁺ and Mg²⁺ into calcite under karst-analogue
928 experimental conditions. *Geochim. Cosmochim. Acta* 65, 47-62.

929 Jamieson, R. A., Baldini, J. U., Frappier, A. B., & Müller, W., 2015. Volcanic ash fall events identified
930 using principal component analysis of a high-resolution speleothem trace element dataset. *Earth*
931 *and Planetary Science Letters*, 426, 36-45.

932 Jamieson, R.A., Baldini, J.U.L., Brett, M.J., Taylor, J., Ridley, H.E., Ottley, C.J., Prufer, K.M., Wassenburg,
933 J.A., Scholz, D., Breitenbach, S.F.M., 2016. Intra- and inter-annual uranium concentration variability
934 in a Belizean stalagmite controlled by prior aragonite precipitation: A new tool for reconstructing
935 hydro-climate using aragonitic speleothems. *Geochim. Cosmochim. Acta* 190, 332-346.

936 Johnson, K.R., Hu, C.Y., Belshaw, N.S., Henderson, G.M., 2006. Seasonal trace-element and stable-
937 isotope variations in a Chinese speleothem: The potential for high-resolution paleomonsoon
938 reconstruction. *Earth Planet. Sci. Lett.* 244, 394-407.

939 Kottek, M., Grieser, J., Beck, C., Rudolf, B., Rubel, F., 2006. World Map of the Köppen-Geiger climate
940 classification updated. *Meteorol. Zeit.* 15, 259-263.

941 Ljungqvist, F.C., Krusic, P.J., Brattstrom, G., Sundqvist, H.S., 2012. Northern Hemisphere temperature
942 patterns in the last 12 centuries. *Clim. Past* 8, 227-249.

943 Ljungqvist, F.C., Krusic, P.J., Sundqvist, H.S., Zorita, E., Brattström, G., Frank, D., 2016. Northern
944 Hemisphere hydroclimate variability over the past twelve centuries. *Nature* 532, 94-98.

945 Lohmann, K.C., 1988. *Geochemical Patterns of Meteoric Diagenetic Systems and Their Application to*
946 *Studies of Paleokarst*, in: N.P. James, P.W. Choquette (Eds.), *Paleokarst*. Springer New York, New
947 York, pp. 58-80.

948 Luterbacher, J., Werner, J.P., Smerdon, J.E., Fernandez-Donado, L., Gonzalez-Rouco, F.J., Barriopedro,
949 D., Ljungqvist, F.C., Buntgen, U., Zorita, E., Wagner, S., Esper, J., McCarroll, D., Toreti, A., Frank, D.,
950 Jungclaus, J.H., Barriendos, M., Bertolin, C., Bothe, O., Brazdil, R., Camuffo, D., Dobrovolny, P.,
951 Gagen, M., Garica-Bustamante, E., Ge, Q., Gomez-Navarro, J.J., Guiot, J., Hao, Z., Hegerl, G.C.,
952 Holmgren, K., Klimenko, V.V., Martin-Chivelet, J., Pfister, C., Roberts, N., Schindler, A., Schurer, A.,
953 Solomina, O., von Gunten, L., Wahl, E., Wanner, H., Wetter, O., Xoplaki, E., Yuan, N., Zanchettin, D.,
954 Zhang, H., Zerefos, C., 2016. European summer temperatures since Roman times. *Environ. Res. Lett.*
955 11, 12.

956 Masson-Delmotte, V., Schulz, M., Abe-Ouchi, A., Beer, J., Ganopolski, A., González Rouco, J.F., Jansen,
957 E., Lambeck, K., Luterbacher, J., Naish, T., Osborn, T., Otto-Bliesner, B., Quinn, T., Ramesh, R., Rojas,
958 M., Shao, X., Timmermann, A., 2013. Information from Paleoclimate Archives, in: Stocker, T.F., Qin,
959 D., Plattner, G.-K., Tignor, M., Allen, S.K., Boschung, J., Nauels, A., Xia, Y., Bex, V., Midgley, P.M.
960 (Eds.), *Climate Change 2013: The Physical Science Basis. Contribution of Working Group I to the*
961 *Fifth Assessment Report of the Intergovernmental Panel on Climate Change.* Cambridge University
962 Press, Cambridge, United Kingdom and New York, NY, USA.

963 Matthey, D., Lowry, D., Duffet, J., Fisher, R., Hodge, E., Frisia, S., 2008. A 53 year seasonally resolved
964 oxygen and carbon isotope record from a modern Gibraltar speleothem: reconstructed drip water
965 and relationship to local precipitation. *Earth and Planetary Science Letters* 269, 80–95.

966 Muller, R.A., MacDonald, G.J., 2000. *Ice Ages and Astronomical Causes: Data, Spectral Analysis and*
967 *Mechanisms.* Springer, London, U.K., pp. 318.

968 Oster, J.L., Montanez, I.P., Mertz-Kraus, R., Sharp, W.D., Stock, G.M., Spero, H.J., Tinsley, J., Zachos,
969 J.C., 2014. Millennial-scale variations in western Sierra Nevada precipitation during the last glacial
970 cycle MIS 4/3 transition. *Quat. Res.* 82, 236-248.

971 Pages 2k Consortium, 2013. Continental-scale temperature variability during the past two millennia.
972 *Nature Geosci.* 6, 339-346.

973 Pas, D., Da Silva, A.C., Devleeschouwer, X., De Vleeschouwer, D., Cornet, P., Labaye, C., Boulvain, F.,
974 2016. Insights into a million-year-scale Rhenohercynian carbonate platform evolution through a
975 multi-disciplinary approach: example of a Givetian carbonate record from Belgium. *Geol. Mag.* 1-
976 33.

977 Pingitore N.E., 1978. The behavior of Zn²⁺ and Mn²⁺ during carbonate diagenesis: theory and
978 application. *Journal of Sedimentary Petrology* 48 (3): 799-814.

979 Pingitore, N.E., Eastman, M.P., 1986. The coprecipitation of Sr²⁺ with calcite at 25 degrees C and 1
980 Atm. *Geochim. Cosmochim. Acta* 50, 2195-2203.

981 Pingitore N.E., Lytle F.W., Davies B.M., Eastman M.P., Eller P.G. and Larson E.M., 1992. Mode of
982 incorporation of Sr²⁺ in calcite: determination by X-ray absorption spectroscopy. *Geochimica et*
983 *Cosmochimica Acta* 56: 1531-1538.

984 PREAT, A., BULTYNCK, P., Brice, D., 2006. Givetian. *Geologica Belgica.*

985 Quinif, Y., 1988. Une nouvelle topographie de la Grotte de Han - Google Scholar. *Lapiaz hors serie*
986 "Special Han" 15–18.

987 Regattieri, E., Zanchetta, G., Drysdale, R. N., Isola, I., Woodhead, J. D., Hellstrom, J. C., ... & Dotsika, E.,
988 2016. Environmental variability between the penultimate deglaciation and the mid Eemian: Insights
989 from Tana che Urla (central Italy) speleothem trace element record. *Quaternary Science Reviews,*
990 152, 80-92.

991 Ridley, H.E., Baldini, J.U.L., Prufer, K.M., Walczak, I.W., Breitenbach, S.F.M., 2015. High-resolution
992 monitoring of Yok Balum Cave, Belize: an investigation of seasonal ventilation regimes and the
993 atmospheric and drip-flow response to a local earthquake. *J. Cave Karst Stud.* 77, 183-199.

994 Rimstidt, J.D., Balog, A., Webb, J., 1998. Distribution of trace elements between carbonate minerals
995 and aqueous solutions. *Geochimica et Cosmochimica Acta* 62, 1851–1863.

996 Roberts, M.S., Smart, P.L., Baker, A., 1998. Annual trace element variations in a Holocene speleothem. *Earth Planet. Sci.*
997 *Lett.* 154, 237-246.

998 Roberts, M.S., Smart, P.L., Baker, A., 1998. Annual trace element variations in a Holocene speleothem.
999 *Earth and Planetary Science Letters* 154, 237–246.

1000 Rozanski, K., Araguasaraguas, L., Gonfiantini, R.,
1001 1992. Relation between long-term trends of O-18 isotope composition of precipitation and climate.
Science 258, 981-985.

1002 Rutledge, H., Baker, A., Marjo, C.E., Andersen, M.S., Graham, P.W., Cuthbert, M.O., Rau, G.C., Roshan,
1003 H., Markowska, M., Mariethoz, G., 2014. Dripwater organic matter and trace element geochemistry
1004 in a semi-arid karst environment: Implications for speleothem paleoclimatology. *Geochimica et*
1005 *Cosmochimica Acta* 135, 217–230.

1006 Smith, C.L., Fairchild, I.J., Spotl, C., Frisia, S., Borsato, A., Moreton, S.G., Wynn, P.M., 2009. Chronology
1007 building using objective identification of annual signals in trace element profiles of stalagmites.
1008 *Quat. Geochronol.* 4, 11-21.

1009 Thornthwaite, C.W., Mather, J.R., 1957. Instructions and Tables for the Computing Potential
1010 Evapotranspiration and the Water Balance. *Publications in Climatology* 10, 311.

1011 Treble, P., Shelley, J.M.G., Chappell, J., 2003. Comparison of high resolution sub-annual records of trace
1012 elements in a modern (1911-1992) speleothem with instrumental climate data from southwest
1013 Australia. *Earth Planet. Sci. Lett.* 216, 141-153.

1014 Van Beynen P.E., Toth V.A., Ford D.C. and Schwarcz H.P., 1997. Seasonal fluxes of humic substances in
1015 cave drip waters, Marengo Cave, Southern Indiana. *Proc. of the 12th Int. Congress of Speleology,*
1016 *Switzerland (2):* 120.

1017 Van Rampelbergh, M., Verheyden, S., Allan, M., Quinif, Y., Cheng, H., Edwards, L.R., Keppens, E.,
1018 Claeys, P., 2015. A 500-year seasonally resolved $\delta^{18}\text{O}$ and $\delta^{13}\text{C}$
1019 sup^{13}C layer thickness and calcite aspect record from a speleothem
1020 deposited in the Han-sur-Lesse cave, Belgium. *Climate of the Past* 11, 789–802.

1021 Van Rampelbergh, M., Verheyden, S., Allan, M., Quinif, Y., Keppens, E., Claeys, P., 2014. Monitoring
1022 of a fast-growing speleothem site from the Han-sur-Lesse cave, Belgium, indicates equilibrium
1023 deposition of the seasonal $\delta^{18}\text{O}$ and $\delta^{13}\text{C}$ signals in the calcite. *Climate of the Past* 10, 1871–
1024 1885.

1025 Verheyden, S., Keppens, E., Fairchild, I.J., McDermott, F., Weis, D., 2000. Mg, Sr and Sr isotope
1026 geochemistry of a Belgian Holocene speleothem: implications for paleoclimate reconstructions.
1027 *Chemical Geology* 169, 131–144.

1028 Verheyden, S., Baele, J.M., Keppens, E., Genty, D., Cattani, O., Hai, C., Edwards, L., Hucai, Z., Van
1029 Strijdonck, M., Quinif, Y., 2006. The proserpine stalagmite (Han-sur-Lesse cave, Belgium):
1030 Preliminary environmental interpretation of the last 1000 years as recorded in a layered
1031 speleothem. *Geol. Belg.* 9, 245-256.

1032 Verheyden, S., Genty, D., Deflandre, G., Quinif, Y., Keppens, E., 2008. Monitoring climatological,
1033 hydrological and geochemical parameters in the Pere Noel cave (Belgium): implication for the
1034 interpretation of speleothem isotopic and geochemical time-series. *Int. J. Speleol.* 37, 221-234.

1035 Wang, Y.J., Cheng, H., Edwards, R.L., An, Z.S., Wu, J.Y., Shen, C.C., Dorale, J.A., 2001. A High-Resolution
1036 Absolute-Dated Late Pleistocene Monsoon Record from Hulu Cave, China. *Science* 294, 2345-2348.

1037 Warken, S. F., Fohlmeister, J., Schröder-Ritzrau, A., Constantin, S., Spötl, C., Gerdes, A., Esper, J., Frank,
1038 N., Arps, J., Terente, M., Riechelmann, D.F.C., Mangini, A., Scholz, D., 2018. Reconstruction of late
1039 Holocene autumn/winter precipitation variability in SW Romania from a high-resolution
1040 speleothem trace element record. *Earth and Planetary Science Letters*, 499, 122-133.

1041 White, W.B., White, E.L., 2013. *Karst hydrology: concepts from the Mammoth Cave area*. Springer
1042 Science & Business Media, New York, USA.

1043 Wynn, P.M., Fairchild, I.J., Spötl, C., Hartland, A., Matthey, D., Fayard, B., Cotte, M., 2014. Synchrotron
1044 X-ray distinction of seasonal hydrological and temperature patterns in speleothem carbonate.
1045 *Environ. Chem.* 11, 28-36.

1046 Zennaro, P., Kehrwald, N., McConnell, J.R., Schupbach, S., Maselli, O.J., Marlon, J., Vallelonga, P.,
1047 Leuenberger, D., Zangrando, R., Spolaor, A., Borrotti, M., Barbaro, E., Gambaro, A., Barbante, C.,
1048 2014. Fire in ice: two millennia of boreal forest fire history from the Greenland NEEM ice core. *Clim.*
1049 *Past* 10, 1905-1924.

1050